FEASIBILITY OF EARLY DAMAGE DETECTION USING SURFACE MOUNTED SENSORS ON EXISTING PAVEMENTS

FINAL PROJECT REPORT

by

Nizar Lajnef
Karim Chatti
Hassene Hasni
Amir H. Alavi

Michigan State University

Sponsorship
Center for Highway Pavement Preservation
(CHPP)

for

Center for Highway Pavement Preservation
(CHPP)

UNIVERSITY TRANSPORTATION CENTER for HIGHWAY PAVEMENT PRESERVATION

In cooperation with US Department of Transportation-Office of the Assistant Secretary for Research and Technology (OST-R)

August 2016

Disclaimer

<table>
<tr><td colspan="4">Technical Report Documentation Page</td></tr>
<tr><td>1. Report No.
CHPP Report-MSU#4-2018</td><td>2. Government Accession No.</td><td colspan="2">3. Recipient's Catalog No.</td></tr>
<tr><td colspan="2" rowspan="2">4. Title and Subtitle
Feasibility of Early Damage Detection Using Surface Mounted Sensors on Existing Pavements</td><td colspan="2">5. Report Date
August 2016</td></tr>
<tr><td colspan="2">6. Performing Organization Code</td></tr>
<tr><td colspan="2">7. Author(s)
Nizar Lajnef, Karim Chatti, Hassene Hasni, Amir H. Alavi</td><td colspan="2">8. Performing Organization Report No.</td></tr>
<tr><td colspan="2" rowspan="2">9. Performing Organization Name and Address

Center for Highway Pavement Preservation,
Tier 1 University Transportation Center
Michigan State University, 2857 Jolly Road, Okemos, MI 48864</td><td colspan="2">10. Work Unit No. (TRAIS)</td></tr>
<tr><td colspan="2">11. Contract or Grant No.
USDOT DTRT13-G-UTC44</td></tr>
<tr><td colspan="2" rowspan="2">12. Sponsoring Organization Name and Address

United States of America
Department of Transportation
Research and Innovative Technology Administration</td><td colspan="2">13. Type of Report and Period Covered</td></tr>
<tr><td colspan="2">14. Sponsoring Agency Code</td></tr>
<tr><td colspan="4">15. Supplementary Notes
Report uploaded at http://www.chpp.egr.msu.edu/</td></tr>
<tr><td colspan="4">16. Abstract

This study presents a self-powered surface sensing approach for detection of bottom-up cracking in asphalt concrete (AC) pavements. The proposed method was based on the interpretation of compressed data stored in memory cells of a self-powered wireless sensor. Different 3D finite element (FE) models of an AC pavement were developed using ABAQUS to generate the sensor output data. A realistic dynamic moving load was applied to the surface of the pavement via DLOAD subroutines developed by FORTRAN. A network of sensing nodes was placed at the top of the AC layer to assess their sensitivity to the progression of bottom-up cracks. Several damage states were defined using Element Weakening Method (EWM). A linear-viscoelastic behavior was considered for the AC layer. In order to detect the damage progression, several damage indicators features were extracted from the data acquisition nodes. The damage detection accuracy was improved through a data fusion model that included the effect of group of sensors. The proposed fusion model was based on the integration of a Gaussian mixture model (GMM) for defining descriptive features, different feature selection algorithms, and a robust and computational intelligence approach for multi-class damage classification. Furthermore, an uncertainty analysis was carried out to verify the reliability of the proposed damage detection approach. The results indicate that the progression of the bottom-up cracks can be accurately detected using the developed intelligent self-powered surface sensing system.</td></tr>
<tr><td colspan="2">17. Key Words: pavement preservation, Pavement management, Structural health monitoring, Smart self-powered sensors, Remaining fatigue life prediction</td><td colspan="2">18. Distribution Statement
No restrictions.</td></tr>
<tr><td>19. Security Classification (of this report)
Unclassified.</td><td>20. Security Classification (of this page)
Unclassified.</td><td>21. No. of Pages

80</td><td>22. Price

NA</td></tr>
</table>

Form DOT F 1700.7 (8-72) Reproduction of completed page authorized

Table of Contents

List of Figures

List of Tables

1. Introduction

Structures health monitoring (SHM) is focused on detection of damage in structures at early stages using advanced technologies. Pavement health monitoring is an extension of the SHM concept that deals with assessing the structural state of pavement infrastructure systems. Distresses concentrated in asphalt concrete (AC) layers can lead to the failure of the pavement structure over time. The maximum tensile stresses are commonly developed at the bottom of the AC layer under repetitive loadings. As a result, cracks usually initiate at the bottom of the asphalt layer and start propagating to the surface of the pavement. This so called bottom-up fatigue cracking is one of the main failure modes in asphalt pavements. The fatigue life of pavements is mainly related to the nature and the amplitude of the applied loading (Miller and Belliger, 2003). A dynamic analysis and a realistic loading modeling are essential to provide accurate prediction of the pavement response. However, most of traditional pavement analysis methods assume a uniform circular loading area and a stationary analysis. Previous studies show that these assumptions may result in an unrealistic pavement response (Cebon, 1986; Yoo and Al-Qadi, 2007). According to a study developed by Cebon (1986), dynamic analysis may increase the fatigue damage and rutting damage by 4 times and at least 40 % respectively. Furthermore, Yoo and Al-Qadi (2007) showed that the dynamic pavement response is usually higher than a quasi-static analysis. In fact, the pavement dynamic response is essentially a function of its natural frequency as well as the external loading frequency. Gillespie et al. (1993) showed that a vehicle speed of 30 mph has a loading frequency of about 4.6 Hz, and 6.5 Hz for 51 mph. Lourens (1992) reported that the magnitude of the stress and deflections in pavement highly depends on the loading frequency and they are different from the results given by a static loading. Yoo and Al-Qadi (2007) concluded that there is about 39 % difference on the tensile strain at the bottom of the asphalt layer between a static and transient dynamic analysis. In addition, flexible pavements are usually modeled as a linear elastic multilayer systems based on the theory of the two-layered elastic systems developed by Burmister in 1943 (Huang 1993). However, hot-mix asphalt (HMA) behaves as a viscoelastic material. This type of material exhibits time, rate and temperature dependency. Al-Qadi et al. (2004) and Elseifi et al. (2006) showed that the approximation of multilayered elastic system underestimates the pavement responses. Furthermore, the HMA mixture behaves as an elastic material only when for low temperature and high loading frequency. Therefore, an efficient pavement modeling should consider both the variation of the loading in time and space, the material on the frequency, and the amplitude of the applied stress.

From a sensing perspective, strain gages are widely used in roadways to detect variations in strains associated with pavement deterioration (Dong et al., 2012; Xue, 2013; Lajnef et al., 2013; Yang et al., 2014). However, the installation of many of the existing sensors demands considerable care during construction. The commonly-used H-shaped strain gages require precise individual placement and wiring systems. To cope with these limitations, recent development in the field of pavement health monitoring has revealed the capabilities of the wireless sensors networks (WSN) (Bennett et al., 1999; Attoh-Okine and Mensah, 2003; Ceylan et al., 2013; Alavi et al., 2016a, Chatti et al., 2016). However, nearly all of the available wireless sensors need an external power supply to activate the sensor. As a consequence, periodic replacement of the sensor battery is needed. This becomes more challenging and sometime impractical for the long-term pavement health monitoring. Therefore, energy harvesting methods have been used to self-power the sensors in structures. One of the most efficient energy harvesting methods is the use of piezoelectric transducers. This family of material has the ability of converting the mechanical energy into an electrical energy by harvesting the micro-strain energy from the structure. Thereafter, by embedding a network of the piezoelectric transducers inside the asphalt pavement layer, they can generate electricity needed to empower the sensor. In this context, a self-powered wireless sensor, previously developed at Michigan State University (MSU) based on the "smart" pebble concept (Huang et al., 2010). Several studies looked at the applicability of this sensor for SHM (Lajnef et al. 2013; Alavi et al. 2016a,b,c). In the pavement health monitoring domain, Lajnef et al. (2013) showed that the pavement fatigue life can be predicted using the sensor. Alavi et al. (2016a) have tested the ability of the sensor for detection and localizing bottom-up cracking in asphalt pavement. In their study, they embedded the sensor inside the AC layer using a spherical epoxy packaging. The sensing system was placed two inches far from the bottom of the layer. Finite element (FE) simulations were also performed to assess the strain amplitude changes due to the bottom-up cracking (Alavi et al. 2016a). The developed FE models were based on an elastic material behavior and a quasi-static loading. Moreover, Alavi et al. (2016a) showed that only the sensors located above the cracks experience a notable change due to the damage progression. However, a disadvantage of embedding the sensors at the bottom of the AC layer is that they may be damaged due to excessive stresses. Furthermore, new pavement construction projects are negligible when compared to the extent of the exiting pavement network. It is thus more critical for State Highway Agencies (SHAs) to adopt monitoring techniques that can be adapted to existing pavements. It should be noted that surface sensing technologies such as remote sensing are commonly used for the monitoring of existing pavements. These methods use the electromagnetic spectrum to identify the surface and subsurface defects. In this context, ground-penetrating radar (GPR) employs the electromagnetic energy to detect subsurface anomalies. GPR can be used for both measuring the pavement thickness and locating voids. GPRs are able to identify cracks and measure cracks depth between 50 to 160 mm in flexible pavements. They can be attached to a service vehicle travelling at highway speed (Zhou et al., 2012). However, major limitations of such methods are that they need notable energy to operate and may not be practical for continuous long-term monitoring purposes.

In order to cope with the limitations of the existing monitoring methods, this study proposes a self-powered wireless surface sensing approach for the detection of the bottom-up cracking in existing asphalt pavements. The propose method would not have major interference with regular pavement maintenance activities. A detailed study was conducted on the minimum spatial distance of the sensors from the damage zone, referred to as resolution, to provide sound detections. A dynamic analysis of a moving truck at highway speed was carried out through a realistic FE modeling. Different damage scenarios were considered by changing the size of the damage zone and the AC material properties. The sensor output was modeled based on the strains extracted from the surface of the AC layer at different sensing nodes. The sensors positions were defined in the longitudinal and transverse directions. Thereafter, features were extracted from the sensor data and fused to define new set of explanatory features. Finally a probabilistic neural network (PNN) classifier was used to classify the predefined damage scenarios.

2. Finite Element Modeling of Pavement Structure Subjected to a Moving Load

2.1. Geometry and FE model

ABAQUS software was employed to simulate the response of the pavement under a moving load. In the FE analysis, the stress/strain response is sensitive to element type and size as well as boundary conditions. In this study, 3D FE models were developed as they are more appropriate compared to a 2D axisymmetric model. In fact, a 3D model allows simulating the contact stresses between the tire footprint and the pavement surface. The pavement model was meshed using two different types of elements: eight-node linear brick elements with reduced integration (C3D8R) and eight node linear infinite elements (CIN3D8). The standard finite elements were used to model the region of interest and the infinite elements were deployed in the far field region. This type of elements allows providing silent boundaries to the FE model in the dynamic analysis and reduces the number of elements at far field (ABAQUS, 2010). These elements have a special shape function to vanish the displacement field when the coordinates approach infinity. Such boundary type can minimize the reflection of the shear and dilatational waves back into the FE mesh (Al-Qadi et al., 2010). In a dynamic analysis, the infinite elements introduce additional normal and shear tractions on the FE boundary using a viscos damping boundary. The introduced normal and shear stresses are proportional to the velocity components as follows (Wang, 2011):

$$\sigma = \rho \, c_p \dot{u} \tag{1}$$

$$\tau = \rho \, c_s \dot{v} \tag{2}$$

where: $\rho, \sigma, \tau c_p, c_s, \dot{u}$ and $\dot{v}$ are the material density, normal stress along the interface between the FE/infinite elements, shear stress along the interface FE/infinite elements, longitudinal wave velocity, shear wave velocity, normal velocity and tangential velocity, respectively. The wave velocities are given by the following expressions (Wang, 2011):

$$c_p = \sqrt{\frac{(1-\nu)E}{(1-2\nu)(1+\nu)\rho}} \tag{3}$$

$$c_s = \sqrt{\frac{E}{2(1+\nu)\rho}} \tag{4}$$

where E and ν are the Young modulus and Poisson's ratio, respectively. In this study, the length of the pavement section was 7 meters in the longitudinal direction (parallel to the traffic direction) and 6 meters in the transverse direction (perpendicular to the traffic direction). The pavement thickness was 6.3 meter. The pavement was composed of three layers: AC, base and subgrade layers. The thickness of the AC, base and subgrade layers are 100 mm, 200 mm and 6000 mm, respectively. Large model dimensions were used to reduce the edge effect and to achieve a full passage of the tire on the pavement. Fig. 1 displays the pavement model as well as the meshed cross section of the AC layer.

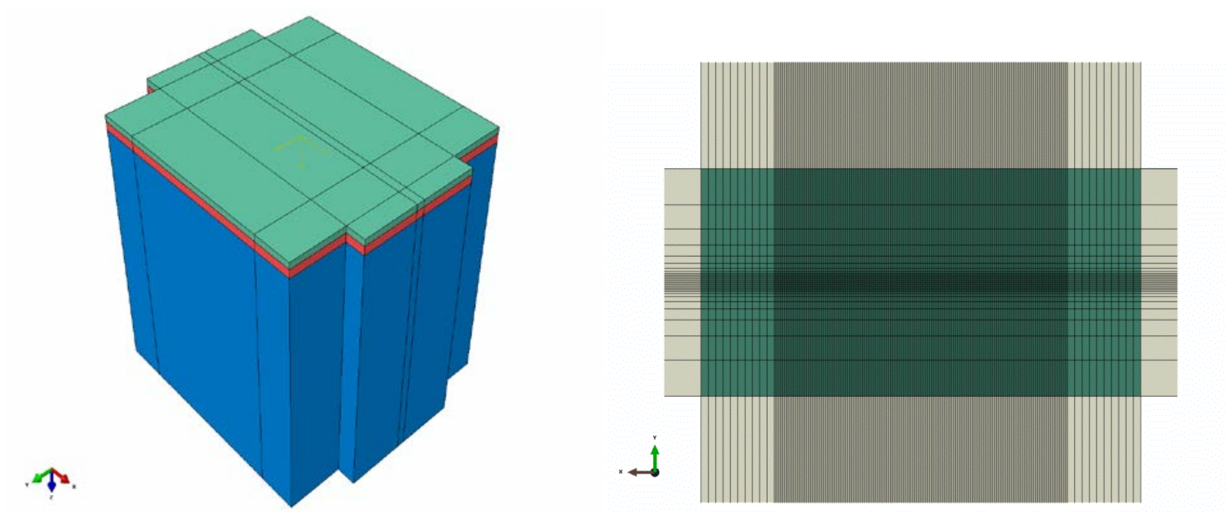

(a) (b)

Figure 1. (a) The 3D FE model of the pavement structure, (b) Meshed cross section of the AC layer

According to a study conducted by Duncan et al. (1968), location of the infinite elements should be at least 12 times the radius of the loading area (R) in the horizontal direction. In this work, the infinite domain was located at approximately 16R from the initial and final location of the load center in the longitudinal direction, and 17R in the transverse direction. The total number of elements was 393,796 elements from dived into 363,440 element of type C3D8R and 30,356 element of type CIN3D8. Fig. 2 displays the structure of CIN3D8. A fine mesh was used around the loading path and a coarse mesh far away from the load. Different simulations were conducted to study the effect of the element dimensions on the pavement response. It was found that an element with dimensions of 20 mm × 20 mm could accurately capture the stress/strain response under the wheel footprint. The element thickness was chosen to be 10 mm for the AC layer, 20 mm for the base and from 20 mm to 500 mm for the subgrade. Furthermore, in a dynamic analysis, it is recommended that the maximum element size should not exceed 1/12 the minimum length of the elastic waves propagating inside the structure. The natural frequency of a typical flexible pavement, the vehicle loading frequency and the stress wave velocity are around 6-14Hz, 0.1-25Hz, and 100 m/s to 600 m/s, respectively. Accordingly, the defined element size is small enough to satisfy the minimum element size requirement.

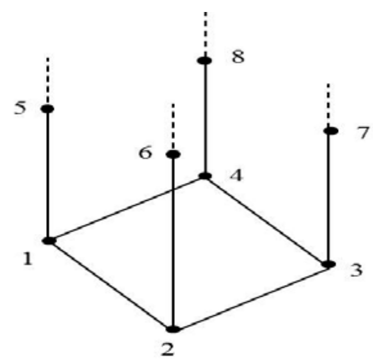

Figure 2. The CIN3D8 element structure

2.2. Dynamic Analysis

For the pavement analysis, the loading can be modeled as a static, quasi-static, or dynamic loading. If the loading is stationary, a static analysis is suitable for the analysis. A quasi-static approach is a sequence of static loads that are moving from one position to another at each time step. Static and quasi-static do not include the effect of inertia forces. However, a dynamic analysis is more appropriate if the load is moving with a certain speed, in which the loading location changes in time and location according to the truck speed,. Therefore, this type of analysis was used in this study. The moving load problem can be treated as structural dynamic problem as it considers slower load changes than wave propagation problems. The response in a wave propagation problem is rich in high frequency mode shapes. The analysis time is also in the order of the wave travel time across the structure. Therefore, a very short step-time is required for this type of analysis. In a structural dynamic problem, the response is dominated by low modes and the effect of high modes is insignificant (Chopra, 2001, Bathe, 1996). If the time required for the stress waves to propagate through the whole structure does not exceed a small portion of the load rise duration, the problem can be assumed to be a structural dynamic problem. As the vehicle speed is much smaller than the stress wave speed (100 m/s to 600 m/s), the problem was treated as a structural dynamic problem in this study. The equation of motion of a multi-degree of freedom system is as given below:

$$M\,\ddot{u} + C\,\dot{u} + K\,u = F \tag{5}$$

where M is the mass matrix, C is the damping matrix, K is the stiffness matrix, u is the displacement vector and F is the external force vector. The first term of the equation $M\,\ddot{u}$ represents the inertia forces and $(C\,\dot{u} + K\,u)$ represents the internal forces.

There are two ways to solve this type of nonlinear equations; an implicit direct integration or an explicit direct integration method. The implicit procedure is more suitable for structural dynamic problems and usually provides good numerical stability. For the method, the displacements at two consecutive times are calculated by solving a set of nonlinear equation simultaneously.

In a dynamic analysis, the selection of the time increment is very important. According to Bathe (1996), the time increment Δt should be less than or equal to $\frac{1}{20\,f_{dominant}}$:

$$\Delta t \;\leq\; \frac{1}{20\,f_{dominant}} \tag{6}$$

where $f_{dominant}$ is dominant frequency of the response of a structure or of the loading. Herein, the time increment was taken 0.001 s which satisfies the time increment requirement as the highest loading frequency is usually lower than 10 Hz.

2.3. Material Characterization

Each layer of the modeled pavement had unique material properties. The HMA layer had viscoelastic properties while an elastic behavior was considered for the base and subgrade layers. The HMA modulus is time (frequency) and temperature dependent. In fact, the state of the stress in the AC layer does not only depend on the current strain but on the entire strain history. The expression of the stress in linear viscoelasticity can be expressed by a Boltzmann superposition integral as follows (Michalczyk, 2011):

$$\sigma(t) = \int_0^t E(t - \tau) \frac{d\varepsilon}{d\tau}\, d\tau \tag{7}$$

In the present study, a generalized Maxwell model was used for representing the linear-viscoelastic behavior of the HMA. This model is a combination of Maxwell elements (one spring and one dashpot) connected in parallel with a spring as shown in Fig 3.

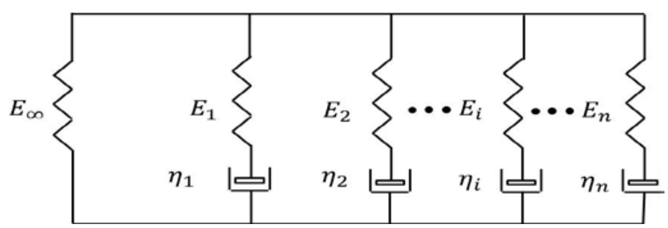

Figure 3. Generalized Maxwell model consisting of n Maxwell elements Connected in parallel

A single element Maxwell model is composed by one spring and one dashpot mounted in series. Therefore, the relationship between the stress-strain is expressed as follows (Michalczyk, 2011):

$$\dot{\varepsilon}(t) = \frac{\dot{\sigma}(t)}{E} + \frac{\sigma(t)}{\eta} \tag{8}$$

where E is the elastic modulus and η is the viscosity parameter.

If the material is suddenly subjected to a deformation ε_0, the solution of the precedent equation becomes:

$$\sigma(t) = E\varepsilon_0 \exp\left(-\frac{t}{\tau}\right) \text{where} \tau = \frac{\eta}{E} \tag{9}$$

where τ represents the relaxation time. By performing a summation over the n Maxwell elements shown in Fig. 3, the stress equation becomes:

$$\sigma(t) = E_\infty \varepsilon_0 + \sum_{i=1}^{n} E_i \varepsilon_0 \exp\left(-\frac{t}{\tau_i}\right) = (E_\infty + \sum_{i=1}^{n} E_i \exp\left(-\frac{t}{\tau_i}\right))\, \varepsilon_0 \tag{10}$$

Therefore, the relaxation modulus:

$$E(t) = \frac{\sigma(t)}{\varepsilon_0} = E_\infty + \sum_{i=1}^{n} E_i \exp\left(-\frac{t}{\tau_i}\right) \tag{11}$$

This expression is a Prony series representation. The equilibrium modulus is E_∞, and the instantaneous modulus E_0 is the value of E(t) at t = 0 given by:

$$E_0 = E_\infty + \sum_{i=1}^{n} E_i \tag{12}$$

By replacing the equilibrium modulus E_∞ by $(E_0 - \sum_{i=1}^{n} E_i)$, Eq. (11) can be rewritten as follows:

$$E(t) = E_0 - \sum_{i=1}^{n} E_i \left(1 - \exp\left(-\frac{t}{\tau_i}\right)\right) \tag{13}$$

Therefore, the Prony series representation is fully defined by (E_i, τ_i). For the FE modeling, ABAQUS uses the dimensionless Prony series representation based on the shear (G) and bulk (K) moduli to define a viscoelastic behavior (Michalczyk, 2011):

$$G(t) = \frac{E(t)}{2\,(1+\nu)} \tag{14}$$

$$K(t) = \frac{E(t)}{3\,(1-2\nu)} \tag{15}$$

If we divide both expressions by the initial values G_0 and K_0 respectively, we obtain:

$$\bar{g}(t) = 1 - \sum_{i=1}^{n} \bar{g}_i \left(1 - \exp\left(-\frac{t}{\tau_i}\right)\right) \tag{16}$$

and:

$$\bar{k}(t) = 1 - \sum_{i=1}^{n} \bar{k}_i (1 - \exp\left(-\frac{t}{\tau_i}\right) \tag{17}$$

Therefore, there are three parameters required in order to define a viscoelastic material property in ABAQUS (Michalczyk, 2011): the dimensionless shear relaxation modulus $\bar{g}_i$, the dimensionless bulk relaxation modulus $\bar{k}_i$, and the relaxation time τ_i. The relaxation modulus of the AC material used in this work was defined by four constants c_i (i=1,2,3,4) from the sigmoid function given by the following expression:

$$Log(E(t)) = c_1 + \frac{c_2}{1+\exp(-c_3 - c_4 \log(t_r))} \tag{18}$$

where t_r is the reduced time, and c_i are coefficients related to the type of the AC material. In this work, the constants c_i were taken as follows:

- C_1 = 0.639
- C_2 = 3.341
- C_3 = 0.709
- C_4 = -0.691

A MATLAB code was developed to fit Eq. (13) to the relaxation modulus given by the sigmoid function (Eq. (18)) in order to obtain the Prony series coefficients. Fig. 4 displays the results of the fitting of the sigmoid function to the Prony representation. On this basis, 33 Prony coefficients were calculated. Thereafter, the dimensionless coefficients $\bar{g}_i$ and $\bar{k}_i$ were obtained based on the Prony coefficients E_i. The instantaneous modulus was calculated based on the equilibrium modulus and the 33 coefficients as expressed by Eq. (19):

$$E_0 = E_\infty + \sum_{i=1}^{33} E_i = 9548\ MPa \tag{19}$$

Table 1 presents the values used for the definition of the viscoelasticity material property for the AC layer. The Poisson's ratio was equal to 0.35.

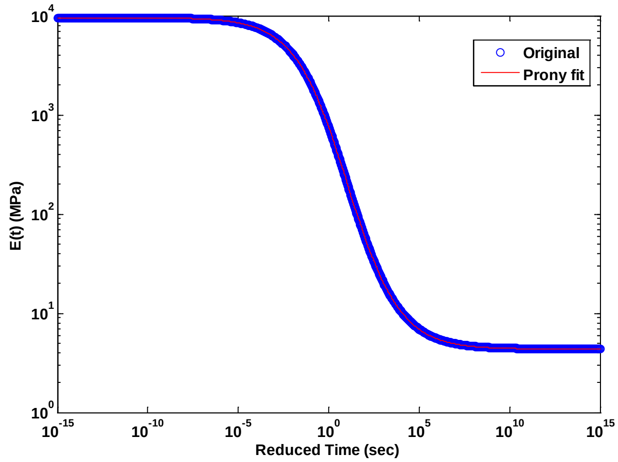

Figure 4. Prony series fitted to the original sigmoid function

For the AC layer, there is no need to define an additional structural damping as it is behaves as a viscoelastic material. However, as the base and the subgrade are elastic materials, it is important to include an additional damping to include the effect of energy absorption when the wave propagates through the soil. Therefore, a 5 % damping ratio was defined for both the base and the subgrade layers. Table 2 presents the material properties of the three pavement layers.

2.4. Loading

2.4.1. Contact Area

Tire-pavement interaction is a complex phenomenon due to the tire footprint, non-uniform contact area, and shear stress components (Siddharthan et al., 1998). A tire footprint consists of many small surfaces contacting the pavement separated by ribs that may not make contact with pavement and thus may not contribute to loading. Defining a tire footprint that simulates a real tire-pavement interaction is possible using the FE modeling. Tielking and Roberts (1987) used the ILLIPAVE finite element pavement program to model non-uniform contact pressures of a tire moving on an asphalt pavement surface. Their tire contact pressure model took into account normal pressure, transverse shear pressure, and longitudinal shear pressure. Their results showed that non-uniform contact pressure induced greater tensile strain at the bottom of the asphalt layer compared to uniform loading.

Table 1. Prony Series Coefficients

$\bar{g}_i$	$\bar{k}_i$	τ_i
0.000367	0.000367	1.00E-13
0.000262342	0.000262342	6.49E-13
0.000678368	0.000678368	4.22E-12
0.00108393	0.00108393	2.74E-11
0.00194552	0.00194552	1.78E-10
0.00338058	0.00338058	1.15E-09
0.00591073	0.00591073	7.50E-09
0.0102785	0.0102785	4.87E-08
0.0177787	0.0177787	3.16E-07
0.0304279	0.0304279	2.05E-06
0.0511115	0.0511115	1.33E-05
0.0829927	0.0829927	8.66E-05
0.126665	0.126665	0.000562
0.172722	0.172722	0.003652
0.193456	0.193456	0.023714
0.159339	0.159339	0.153993
0.0891806	0.0891806	1
0.0349519	0.0349519	6.49382
0.0112675	0.0112675	42.1697
0.00355265	0.00355265	273.842
0.00124161	0.00124161	1778.28
0.000492694	0.000492694	11547.8
0.000222137	0.000222137	74989.4
0.000108642	0.000108642	486968
5.68027e-05	5.68027e-05	3.16E+06
3.06136e-05	3.06136e-05	2.05E+07
1.69927e-05	1.69927e-05	1.33E+08
9.44883e-06	9.44883e-06	8.66E+08
5.45866e-06	5.45866e-06	5.62E+09
2.83722e-06	2.83722e-06	3.65E+10
2.16651e-06	2.16651e-06	2.37E+11
1.00153e-07	1.00153e-07	1.54E+12
1.83335e-06	1.83335e-06	1.00E+13

Table 2.Material properties

Layer	Modulus(MPa)	Poisson's ratio	Density (Kg/m^3)	Damping (%)
HMA	9548	0.35	2325	-
Base	193	0.3	2000	5
Subgrade	43	0.4	1500	5

However, simplifying the contact area can affect the pavement strain response since the distribution of the stress field in the contact zone can affect the pavement response (Tielking and Roberts, 1987; Wang and Machemehl, 2006; Yue and Svec, 1995). Tire pressure and load intensity affect contact pressure distribution (Tielking and Roberts, 1987; Alkasawneh et al., 2008; Mun et al., 2006; Weissman, 1999; Perret and Dumont, 2004). In the multilayered elastic theory, the shape of the tire footprint is assumed to have a circular shape as it conserves the property of an axisymmetric problem. Wang and Machemehl (2006) showed that the assumption of a uniform circular tire-pavement pressure area can underestimate the vertical compressive e strains at the top of the subgrade and overestimate the tensile strains at the bottom of the AC layer. In most of the 3D FE modeling of pavement, the contact area between a tire and the pavement surface is approximated as a rectangle with two semi-circles as shown in Fig.5.

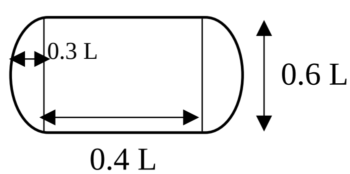

Figure 5. Tire contact area

In this work, the contact area was assumed to be rectangular. The obtained contact area was transformed to a simple rectangle with the same width 0.6 L. The area of the contact area shown in Fig. 5 is equal to:

$$A_c = 0.4\ L \times 0.6\ L + 2 \times \left(\frac{\pi\ (0.3\ L)^2}{2}\right) = 0.5227\ L^2 \tag{20}$$

Therefore, if a denotes the length of the equivalent rectangle, the area of the equivalent rectangle (Fig.6) is:

$$A_c = a \times 0.6\, L = 0.5227\, L^2 \tag{21}$$

which gives: $a = \frac{0.5227\, L^2}{0.6\, L} = 0.8712\, L$

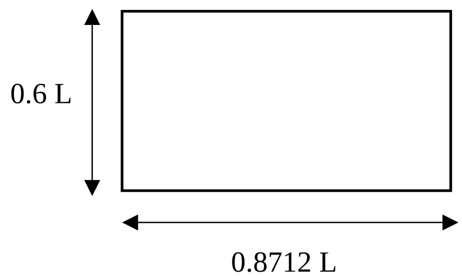

Figure 6. Approximated rectangular loading

The area of the contact area used in this work is $A_c = 0.0260\ m^2$. Therefore L is given by:

$$L = \sqrt{\frac{A_c}{0.5227}} = \sqrt{\frac{0.0260}{0.5227}} = 0.2230\, m \tag{22}$$

Thus, the dimensions of the rectangle are: 0.8712 L = 0.1943 m and 0.6 L = 0.1338 m.

2.4.2. Contact Pressure

The loading of the pavement occurred in the center strip of the section. Fig. 7 highlights the loaded strip. In order to simulate the movement of the load at the desired speed, a user defined DLOAD subroutine was developed using FORTRAN. In fact, regular loading functions in ABAQUS do not allow varying the location of the applied load as a function of time. In order to overcome this problem, different approaches were proposed. The load and its amplitude can be shifted over the loading path at each step until a single wheel pass is completed (Al-Qadi and Wang, 2010; Alavi et al., 2016a). This approach is time consuming as it needs the definition of the footprint areas for each step. However, the DLOAD subroutine can be used to define the variation of the distributed load magnitude as function of the position, time, element number and load integration point number (ABAQUS, 2010).

The script specifies the center of the rectangular loading area and its dimensions, the initial and final position of the truck, the truck speed and the tire pressure. A highway speed of 67 mph (30 m/s) was inputted to the FORTRAN code and a tire pressure of 862 kPa was applied. The location of the center of the contact area was calculated by the DLOAD subroutine in each time step as follows:

$$x = v_x \times t + x_0 \tag{23}$$

$$y = v_y \times t + y_0 \tag{24}$$

where v_x, v_y, x_0 and y_0 are the speed in x direction, the speed in the y direction, the x-coordinate of the initial location of the tire center and the y-coordinate of the initial location of the tire center. The vehicle speed was kept constant.

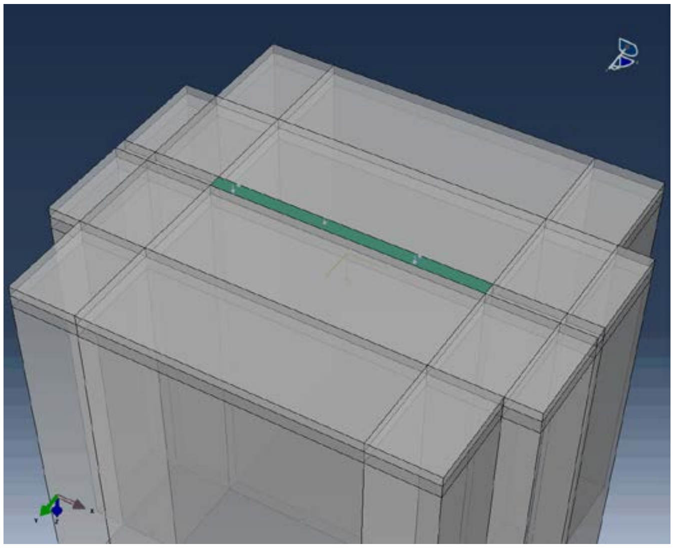

Figure 7. Loaded strip of the AC pavement section

In this work, the loading was assumed to follow the x-axis, therefore, $v_y$was set to zero. The chosen length of the vehicle path is 3 m. As the selected time step of the dynamic analysis was 0.001 second, the tire progresses by:

$$\Delta x_{time-step} = v\,\Delta t = 30\ \times 0.001 = 0.03\,m = 30\,mm \tag{25}$$

As the size of the element around the loading path is 20mm x 20mm, only one element was loaded in each time step.

2.5. Crack Modeling

Many recent studies on flexible pavement fatigue have been conducted using the FE softwares such as Abaqus and FEP++ (Huang et al., 2011; Mun et al., 2006, Sarkar, 2015, Shafabakhsh et al., 2015; Dave and Buttlar, 2010). These programs allow the user to define various complex parameters such as the viscoelastic properties of asphalt. A limitation of using the FE programs for the asphalt pavement analysis pertains to the definition of highly complex scenarios such as fatigue cracking. Fatigue cracking can begin as either a bottom-up crack, top-down crack, or a combination of the two. After repeated loading of the asphalt pavement, crack propagation and additional crack growth further weaken the pavement. These cracks that begin at one end can either continue growing through the thickness of the pavement or coalesce with a different crack growing in another direction. Modeling fatigue cracking inadequately can result in overestimation of fatigue life (Mun et al., 2006). Major factors affecting fatigue cracking are asphalt properties, asphalt thickness, and tire pressure among others. Generally, top-down cracking increases in thicker asphalt, stiffer asphalt, less stiff base and/or subgrade, and under non-uniform loading (Mun et al., 2006).

ABAQUS allows the user to define certain properties by a user subroutine (ABAQUS, 2010). Detailed crack modeling is typically defined using a user subroutine in order to realize more realistic results due to limitations in the basic modeling methods. Cracks defined in ABAQUS using basic modeling for asphalt pavement yield inaccurate results due to over simplification of the crack. Modeling a crack in ABAQUS can be done using extended finite element method (XFEM). Two major limitations that deter XFEM usage in the fatigue cracking pavement analysis are that the method is only viable in static cases and there is no crack growth. Creating a user subroutine to accurately model fatigue cracking in asphalt has yet to be accomplished. Song et al. (2006) have developed a user subroutine of a cohesive fracture model that successfully replicated cracking in asphalt concrete. Dave and Buttlar (2010) have successfully modeled thermal reflective cracking using a user-defined bilinear cohesive crack model. A crack can also be introduced using Element Weakening Method (EWM). Mishnaevsky Jr. (2004) has used this method to simulate the reduced properties resulting from cracking of particle reinforced composites.

In this work, the EWM was also used to introduce the damage to the pavement. Different scenarios were defined based on both the weakening state of the elements defining the damage zone and its height. On this basis, the element elastic modulus was reduced to a certain value in order to define a damage zone. A total of 13 damage states were studied which include 4 different cases of modulus reduction, each having three varying damage zone heights. A damage squared area of 120 mm × 120 mm (6 × 6 elements) was created at the bottom center of the HMA layer. The modulus of this area was reduced 30%, 50%, 70%, and 90% from the instantaneous modulus of the HMA layer. The damage zone heights were 20 mm, 40 mm, and 60 mm. Fig. 8 shows the damage location, cross section, and the measurement locations.

The defined damage states are as given below:

- Intact: Corresponding to the intact configuration,
- D20W30: The damage zone height is 20 mm and the modulus is reduced to 30 % of its initial value,
- D20W50: The damage zone height is 20 mm and the modulus is reduced to 50 % of its initial value,
- D20W70: The damage zone height is 20 mm and the modulus is reduced to 70 % of its initial value,
- D20W90: The damage zone height is 20 mm and the modulus is reduced to 90 % of its initial value,
- D40W30: The damage zone height is 40 mm and the modulus is reduced to 30 % of its initial value,
- D40W50: The damage zone height is 40 mm and the modulus is reduced to 50 % of its initial value,
- D40W70: The damage zone height is 40 mm and the modulus is reduced to 70 % of its initial value,
- D40W90: The damage zone height is 40 mm and the modulus is reduced to 90 % of its initial value,
- D60W30: The damage zone height is 60 mm and the modulus is reduced to 30 % of its initial value,
- D60W50: The damage zone height is 60 mm and the modulus is reduced to 50 % of its initial value,
- D60W70: The damage zone height is 60 mm and the modulus is reduced to 70 % of its initial value,

- D60W90: The damage zone height is 60 mm and the modulus is reduced to 90 % of its initial value.

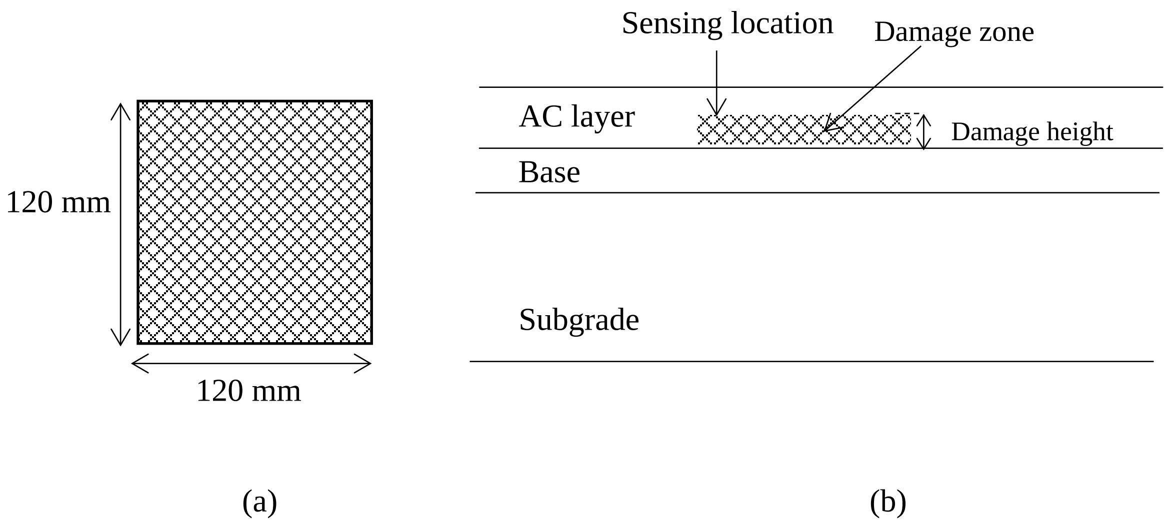

Figure 8. (a) Cross section of the damage (b) Crack zone and measurement location

2.6. Sensors Location

Four rows of eights surface elements, representing sensors, were placed running longitudinally along one side of the pavement section. Each row of sensor elements was offset from the next row in the transverse direction by 60 mm. Sensor 1 was placed in the center of the pavement section and sensors were spaced at 200 mm from one another in the direction of tire loading. Figs 9-11 show the sensor locations. Sensor elements at 0 mm and 60 mm offset have matching element dimensions. Meshing becomes coarser farther away from the tire load path. Thus, sensor elements at 120 mm and 180 mm offset have large, rectangular dimensions when compared with the sensor elements closer to the center load path. Each of the sensor element rows were saved as element sets and assigned to save values of longitudinal strain (E11), transverse strain (E22), and 3D principal strain (EP1, EP2, EP3).

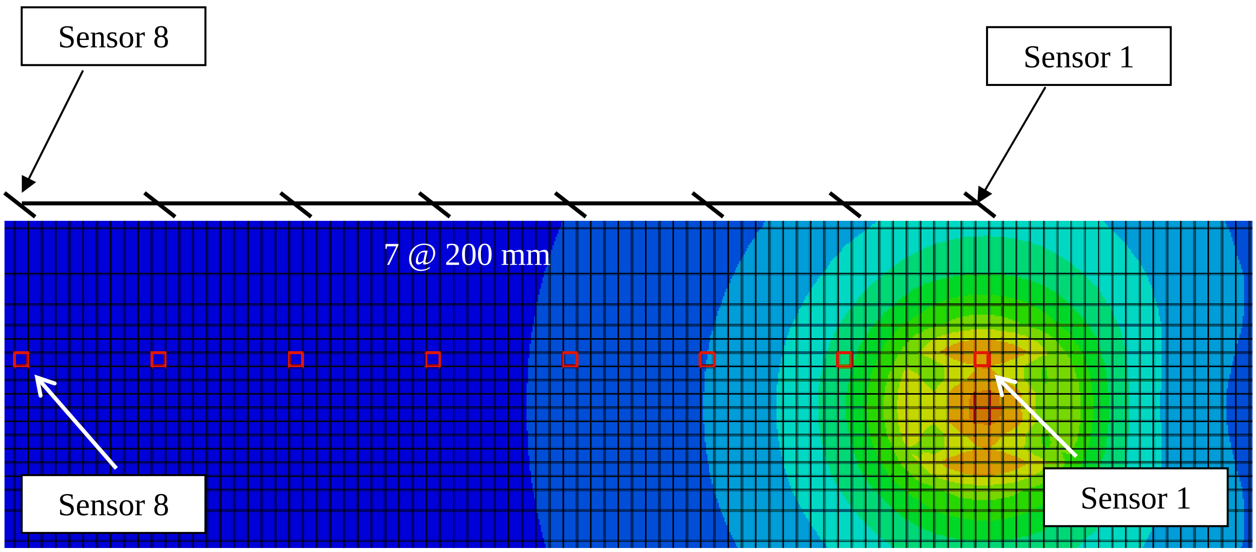

Figure 9. Sensors at 60mm Offset from Center.

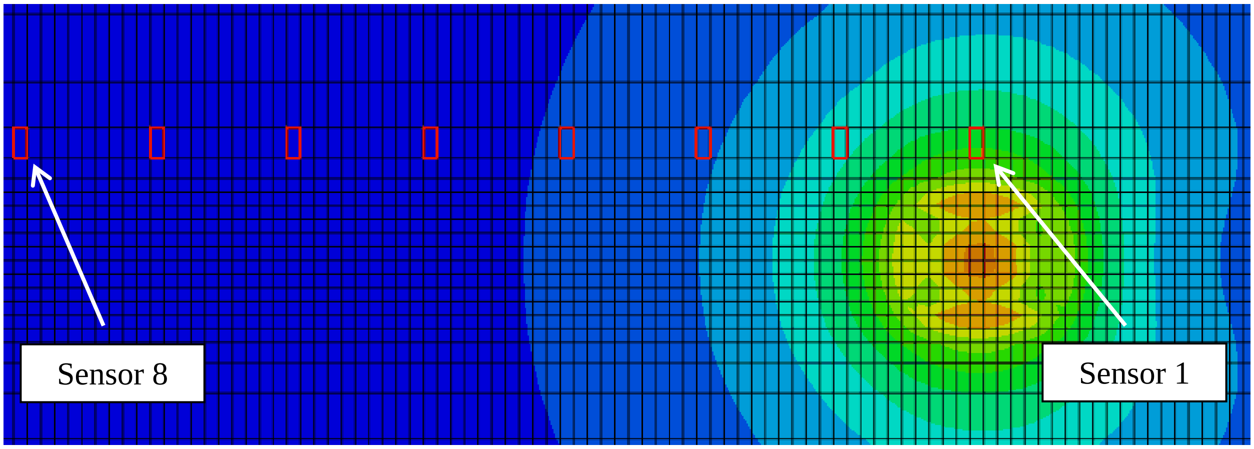

Figure 10. Sensors at 120 mm Offset from Center.

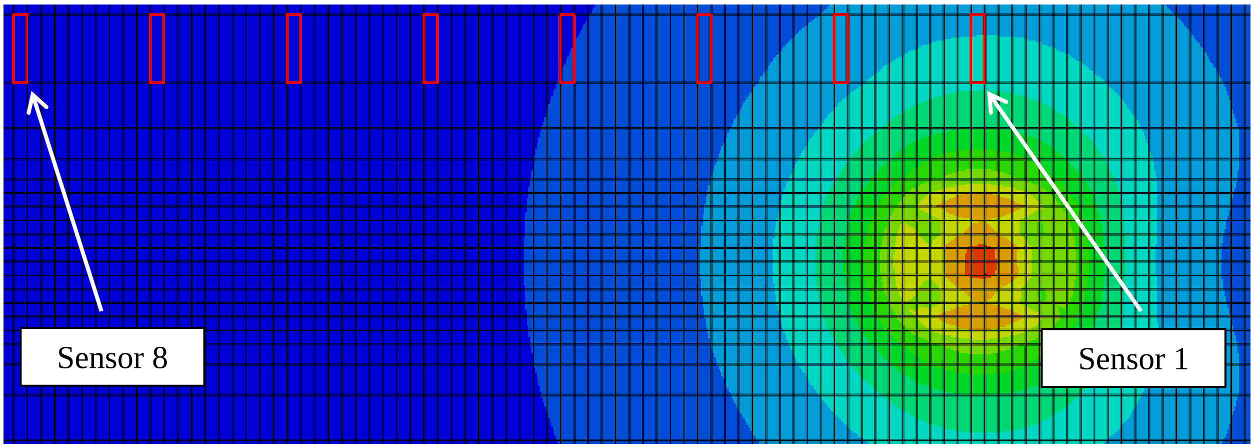

Figure 11. Sensors at 180 mm Offset from Center

Fig. 12 shows the location of the data acquisition nodes on the surface of the AC layer. A set of 32 elements were selected as the sensing nodes. The set was divided into 4 groups (Fig. 9). Each group contained 8 sensing nodes.

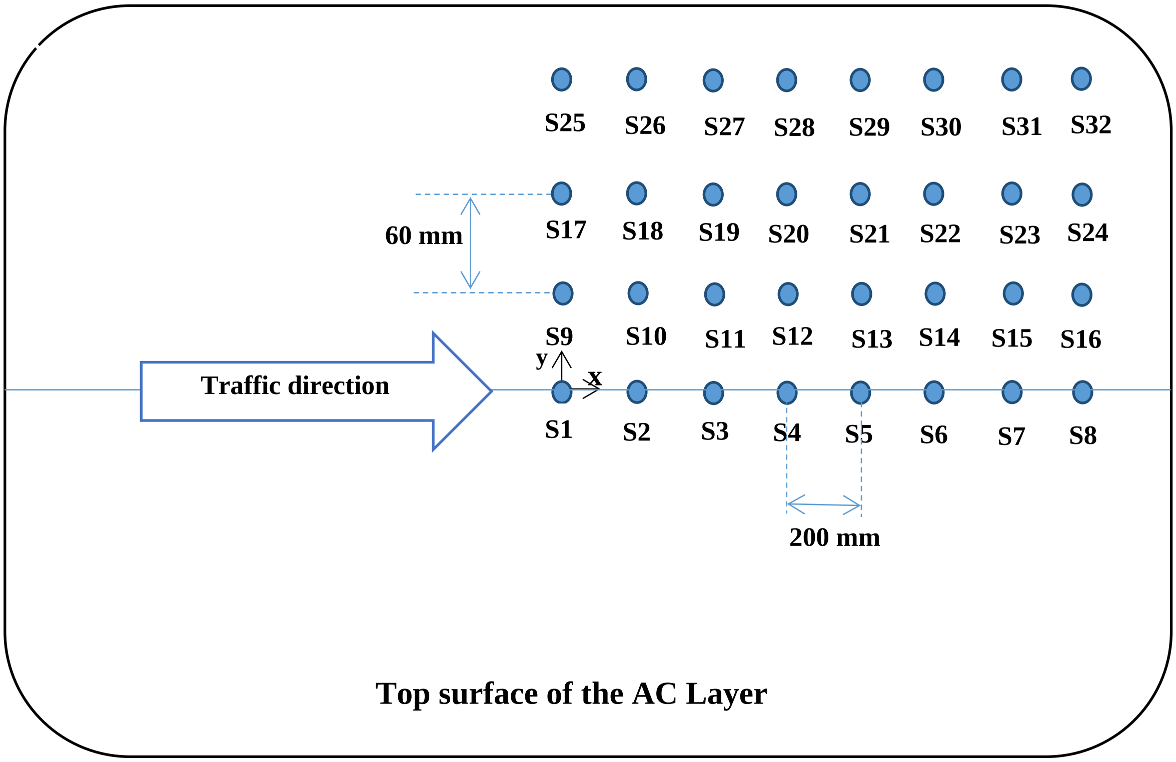

Figure 12. Sensors locations

In each set, the first sensors was located at y = 0 and the distance between two consecutive elements was 200 mm. The transversal distance between two sets was 60 mm. Therefore, the offset of the sets from the center of the pavement (y = 0) was considered as follows:

- Set 1: y = 0
- Set 2: y = 60 mm
- Set 3: y = 120 mm
- Set 4: y = 180 mm

The longitudinal, transverse and principal strains (ε_1,ε_2,ε_3) for each of the predefined damage cases were subsequently extracted.

2.7. The FE Results

2.7.1 Intact Simulations

Figs. 13-15 show the time-history response of the transverse strain for the four rows of sensors in the Intact case. All sensors display equivalent amplitudes corresponding to their distance from the center in the transverse direction (y axis). Sensors located closest to the tire load show higher transverse strain compression peaks. Strain response of Figs. 13 and 14 does not exhibit a similar behavior to the strain response of Figs.16. This is due to the larger element dimensions and rectangular shape of the sensor elements. As a result, strain values from sensor elements located 120 mm and 180 mm away from the center of the pavement in the transverse direction were not investigated further. Furthermore, particular attention was given toward areas exhibiting high strain.

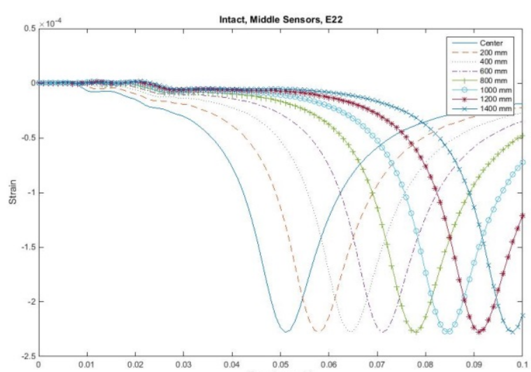

Figure 13. Intact, Middle Sensors, E22

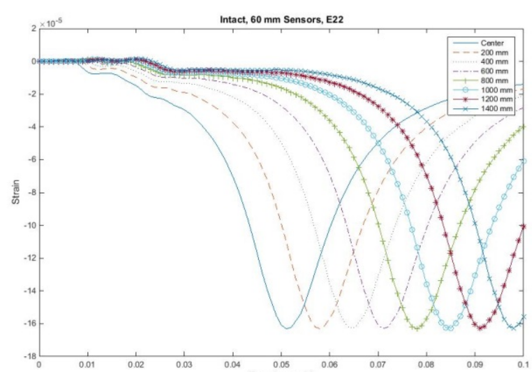

Figure 14. Intact, 60 mm Sensors, E22

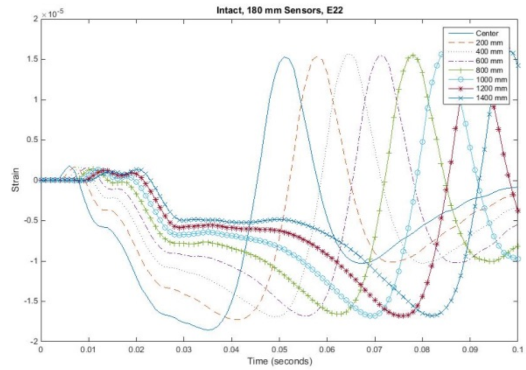

Figure 15. Intact, 180 mm Sensors, E22

2.7.2. Reduced Modulus: 30%

Figs. 16-18 show the transverse strain response of the sensor elements located along the center of the pavement for the 20 mm, 40 mm, and 60 mm damage modes in the 30% reduced modulus case. The sensor element closest to the damage has a much larger variation in strain response than the seven other sensor elements. Compressive transverse strain near the damage zone increases as damage size increases.

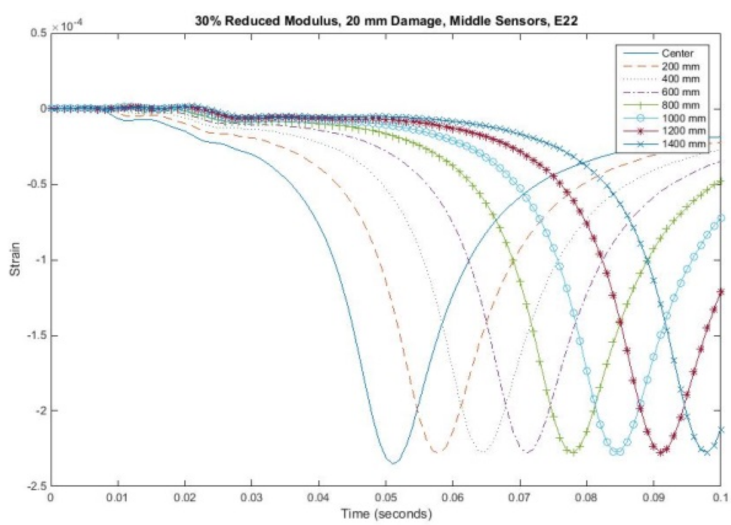

Figure 16. 30% Reduced Modulus, 20 mm Damage, Middle Sensors, E22.

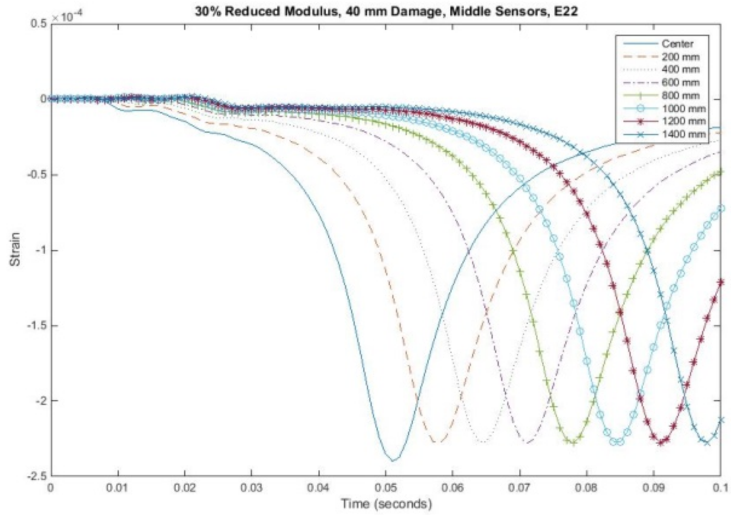

Figure 17. 30% Reduced Modulus, 40 mm Damage, Middle Sensors, E22.

Figs. 19-21 show the transverse strain response of the sensor elements located 60 mm offset from the center of the pavement for the 20 mm, 40 mm, and 60 mm damage modes in the 30% reduced modulus case. Again, the sensor element closest to the damage has a much larger variation in strain response than the seven other sensor elements. Compressive transverse strain near the damage zone decreases as damage size increases.

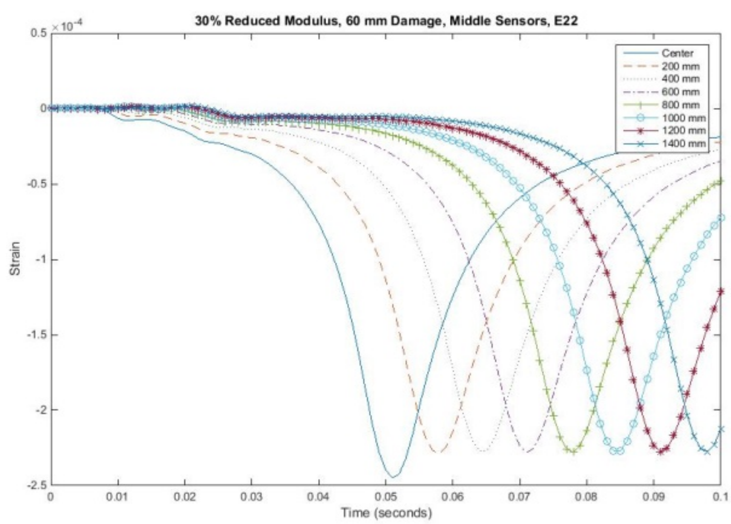

Figure 18. 30% Reduced Modulus, 60 mm Damage, Middle Sensors, E22.

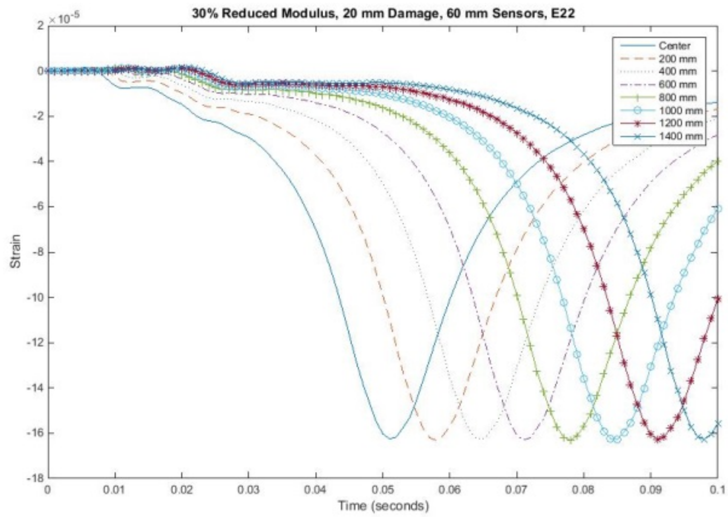

Figure 19. 30% Reduced Modulus, 20 mm Damage, 60 mm Sensors, E22.

Figs. 22-25 show the two sensor elements closest to the damage zone. Sensor 1 in both the Middle location and 60 mm offset location display the most significant variation in transverse strain as damage length progresses. In the Middle location, Sensor 1 exhibits an increase in the compressive transverse strain as damage length increases. There is small variation in the strain for all damage modes in Sensor 2. In the 60 mm offset location, Sensor 1 shows a decrease in the compressive transverse strain as damage length increases. Sensor 2 displays small variation in strain for all damage modes.

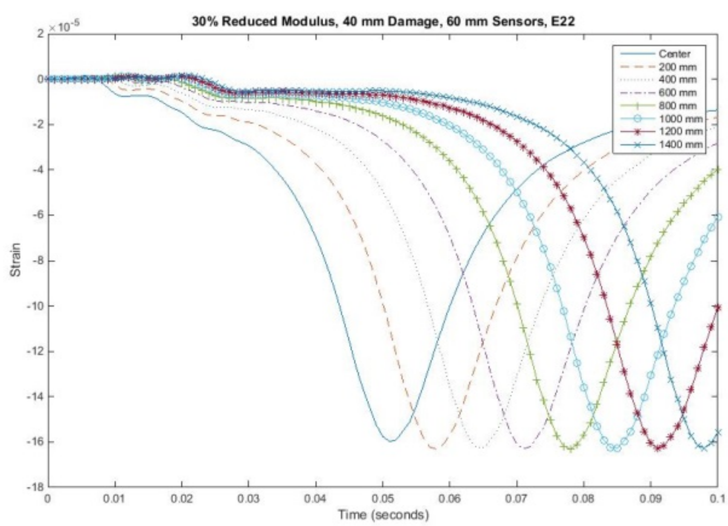

Figure 20. 30% Reduced Modulus, 40 mm Damage, 60 mm Sensors, E22.

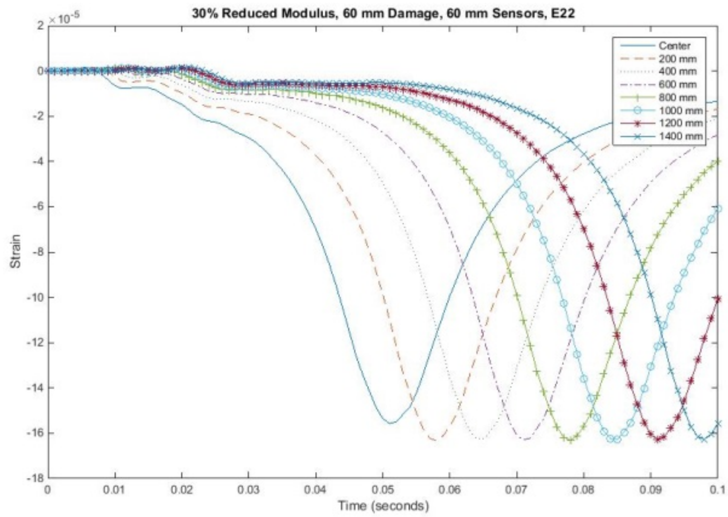

Figure 21. 30% Reduced Modulus, 60 mm Damage, 60 mm Sensors, E22.

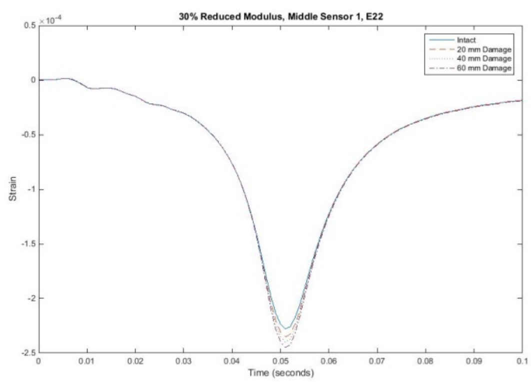

Figure 22. 30% Reduced Modulus, Middle Sensor 1, E22

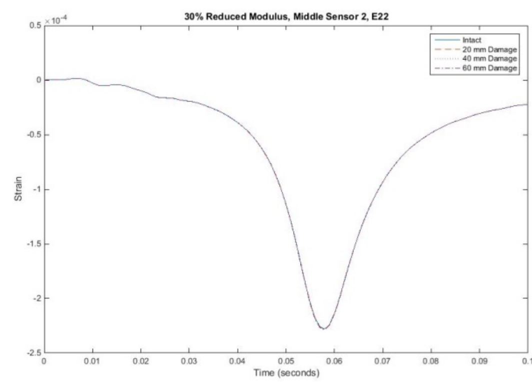

Figure 23. 30% Reduced Modulus, Middle Sensor 2, E22

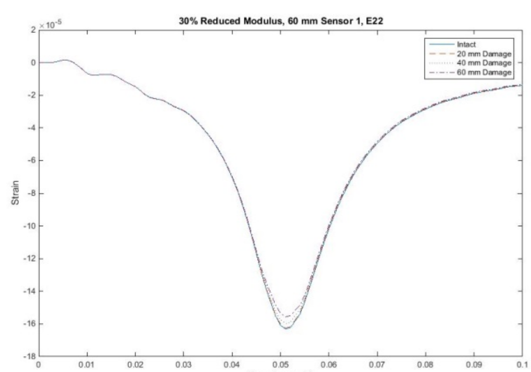

Figure 24. 30% Reduced Modulus, 60 mm Sensor 1, E22

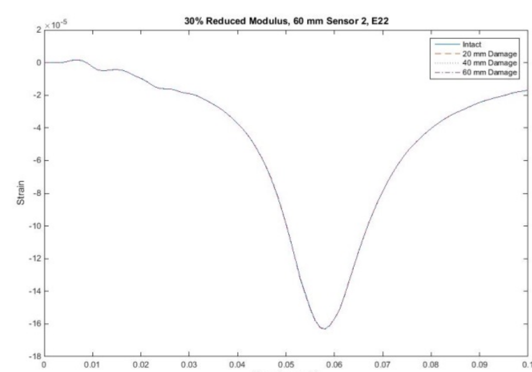

Figure 25. 30% Reduced Modulus, 60 mm Sensor 2, E22

2.7.3. Reduced Modulus: 50%

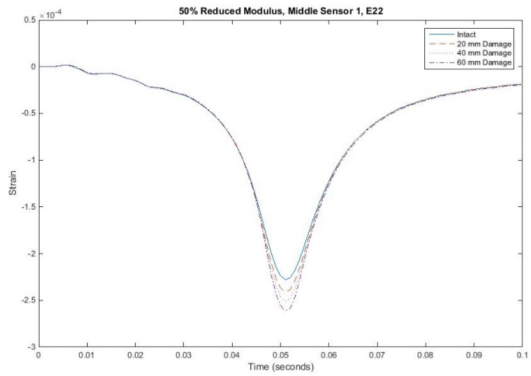

Figure 26. 50% Reduced Modulus, Middle Sensor 1, E22

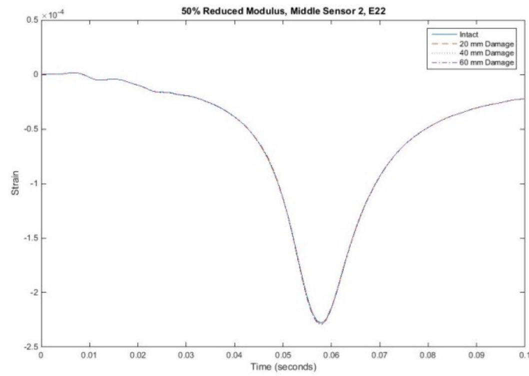

Figure 27. 50% Reduced Modulus, Middle Sensor 2, E22

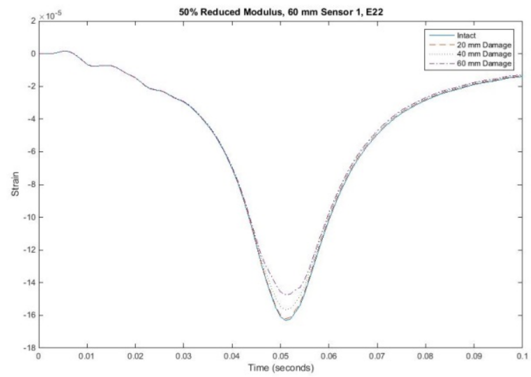

Figure 28. 50% Reduced Modulus, 60 mm Sensor 1, E22

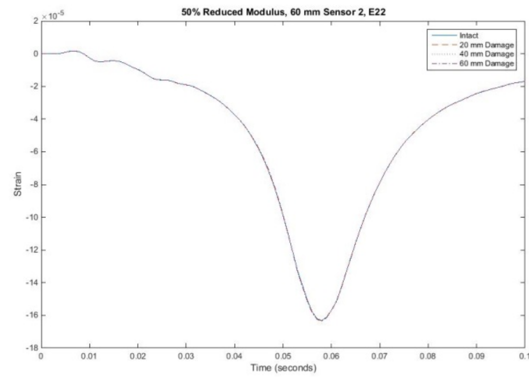

Figure 29. 50% Reduced Modulus, 60 mm Sensor 2, E22

2.7.4. Reduced Modulus: 70%

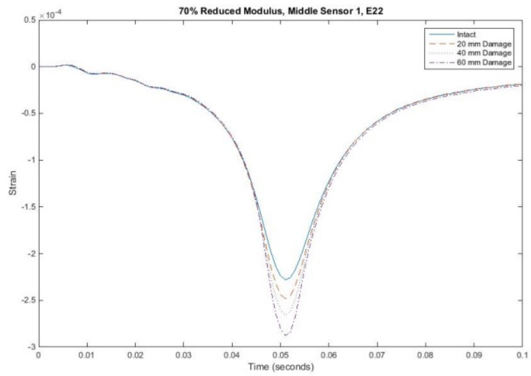

Figure 30. 70% Reduced Modulus, Middle Sensor 1, E22

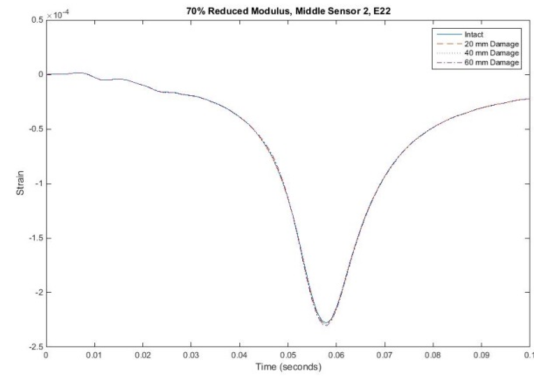

Figure 31. 70% Reduced Modulus, Middle Sensor 2, E22

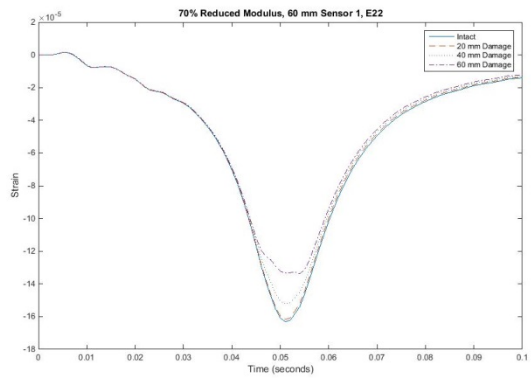

Figure 32. 70% Reduced Modulus, 60 mm Sensor 1, E22

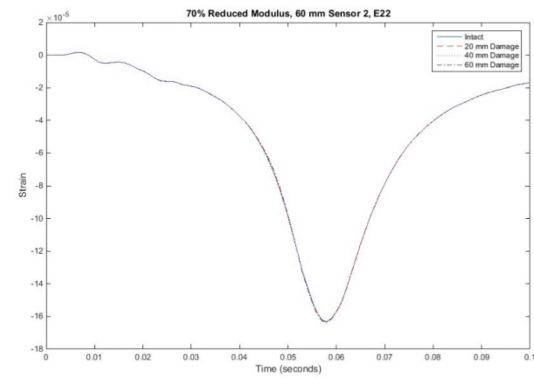

Figure 33. 70% Reduced Modulus, 60 mm Sensor 2, E22

2.7.5. Reduced Modulus: 90%

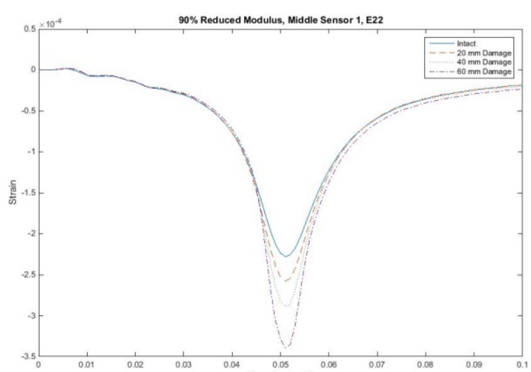

Figure 34. 90% Reduced Modulus, Middle Sensor 1, E22

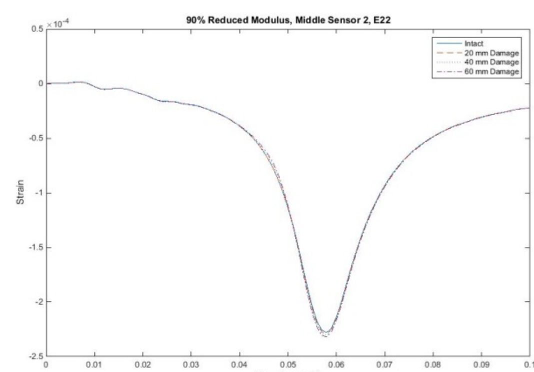

Figure 35. 90% Reduced Modulus, Middle Sensor 2, E22

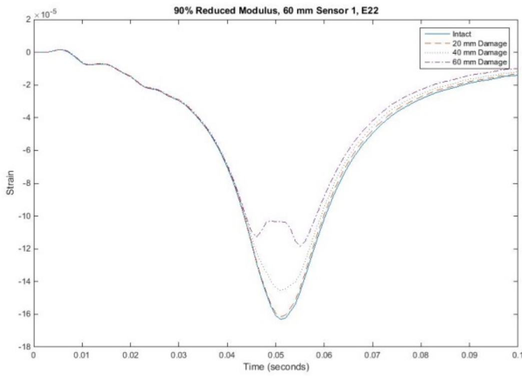

Figure 36. 90% Reduced Modulus, 60 mm Sensor 1, E22

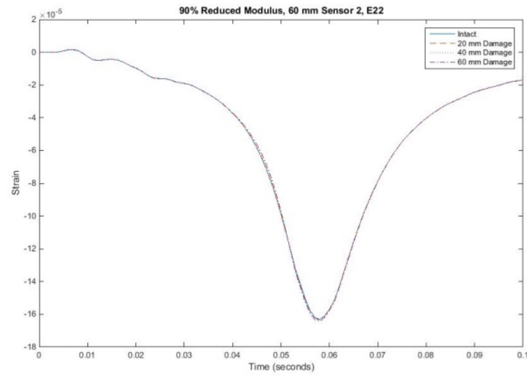

Figure 37. 90% Reduced Modulus, 60 mm Sensor 2, E22

2.7.6. Maximum Strain vs Damage Mode

Results point toward a focus on the sensor elements closest to the damage zone. To this end, the following results highlight the differences in maximum strain values at the four sensor elements located closest to damage. Fig. 38 places a box around the location of the four sensor elements.

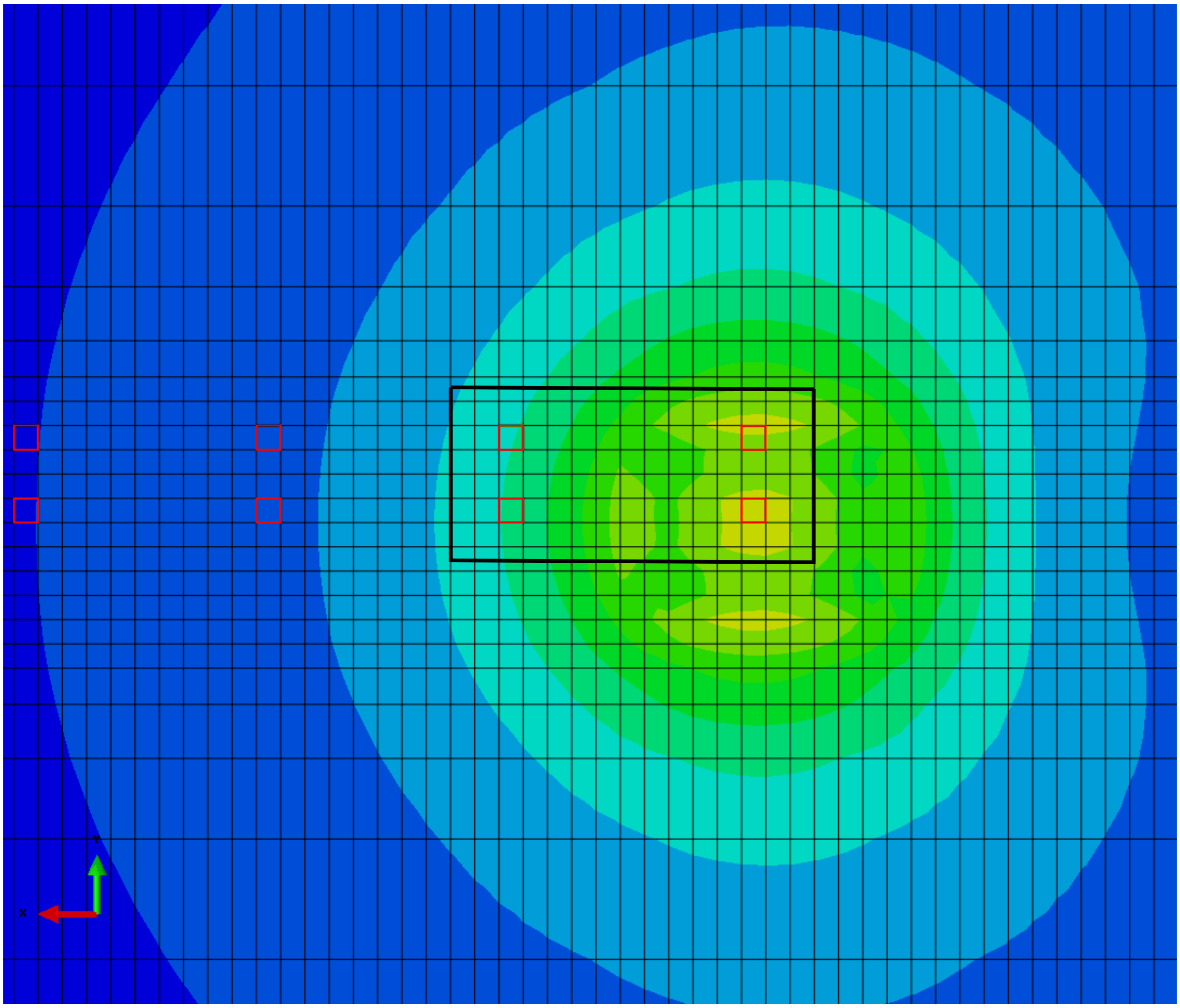

Figure 38. Four Sensor Elements.

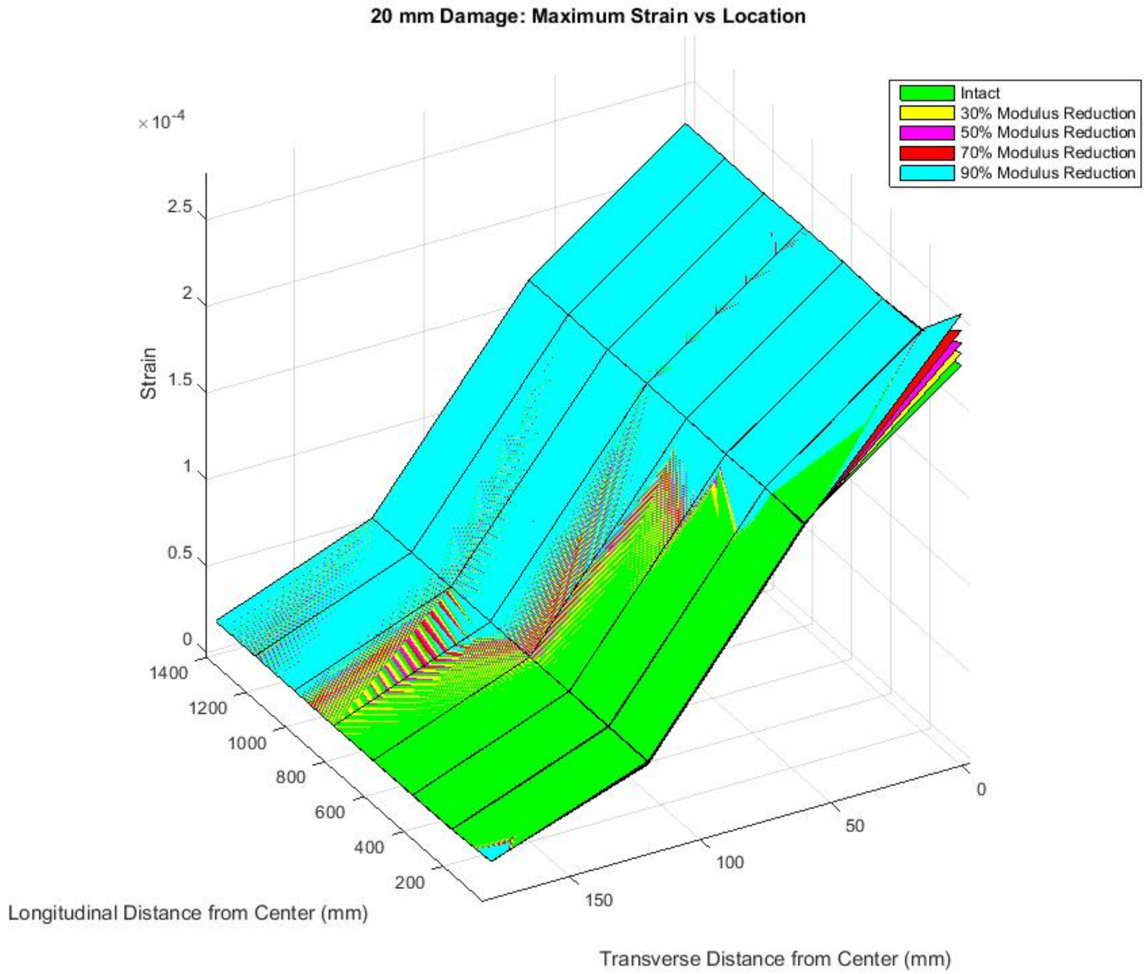

Figure 39. 20mm Damage: Maximum Strain vs Location.

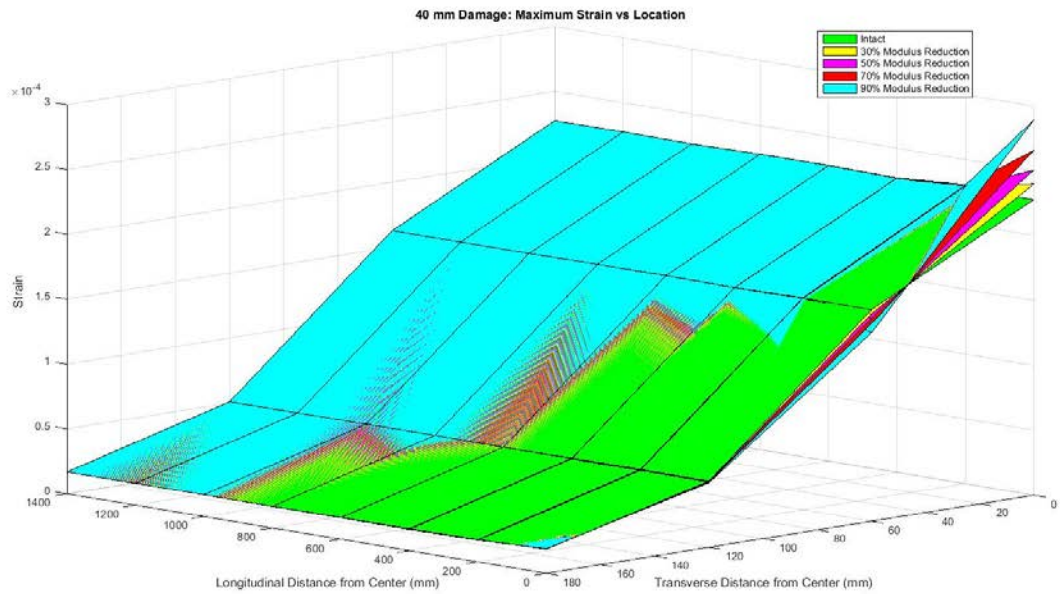

Figure 40. 40mm Damage: Maximum Strain vs Location.

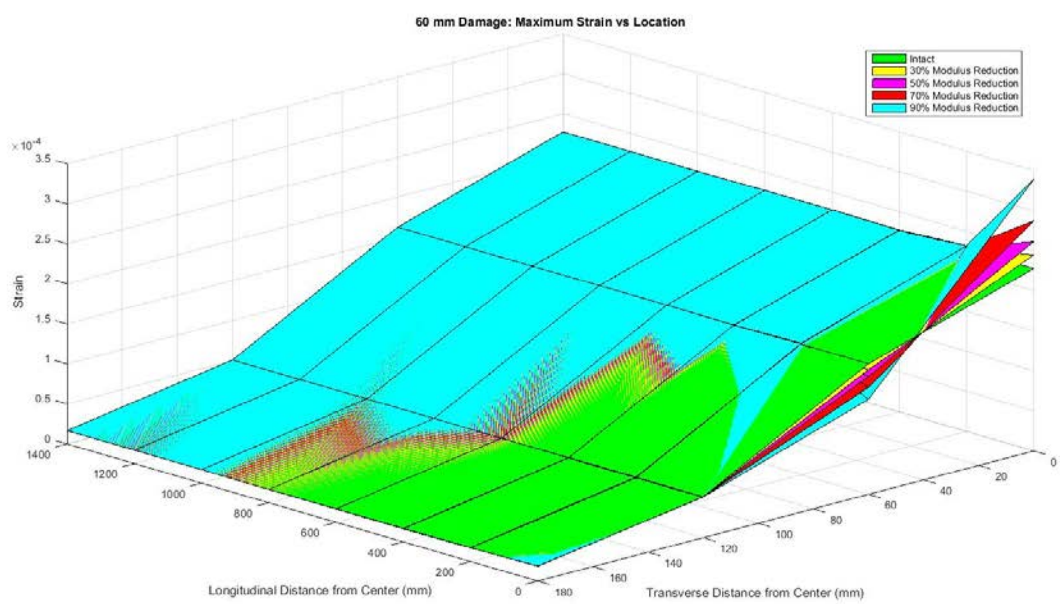

Figure 41. 60mm Damage: Maximum Strain vs Location.

Fig. 42 shows the time history of the first principal strains (in absolute value) for different sensors and for the intact, D20W90, D40W90 and D60W90 damage states. As it seen, for sensor S1, which is located above the damage zone, the amplitude of the strains is much higher than the other sensors. Moreover, as the damage progresses from the intact to the 60 mm damage height, the amplitude of the first principal strains increases as well. The difference of the amplitudes between the Intact and the D60W90 damage state is 111.7 $\mu\varepsilon$.

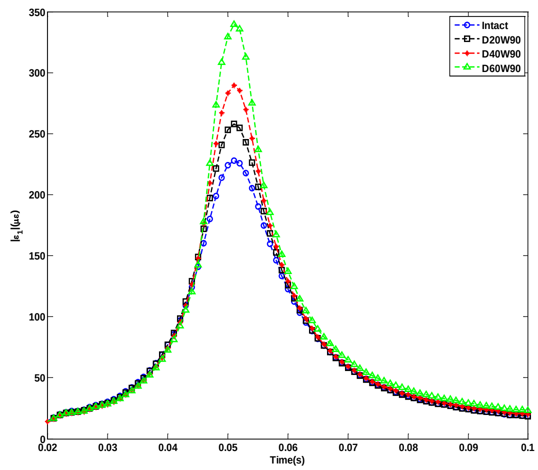

Figure 42. Strain history of sensor S1 for different damage states

Fig. 43 displays the results for sensor S2. Evidently, the difference of the maximum principle strains is being reduced comparing to sensor S1 as the sensor is located at a 200 mm offset from the center of the damage zone. Fig. 44 shows a closer view of the peak values for sensor S2. Fig. 45 displays the results for sensor S17 which is located at x = 0 and at y = 120 mm. As it seen, the amplitude of the strain is changing between damage states but it does not have an increasing trend as for sensors S1 and S2 (Fig. 46). However, for sensor S18 which has a 120 mm offset from the x-axis and 200 mm offset from the y-axis, the strain amplitude continuously increases as the damage progresses (Fig.47). Based on the results, it can be concluded that the amplitude of the strains is affected by the damage states as well as the location of the sensor with respect to the damage.

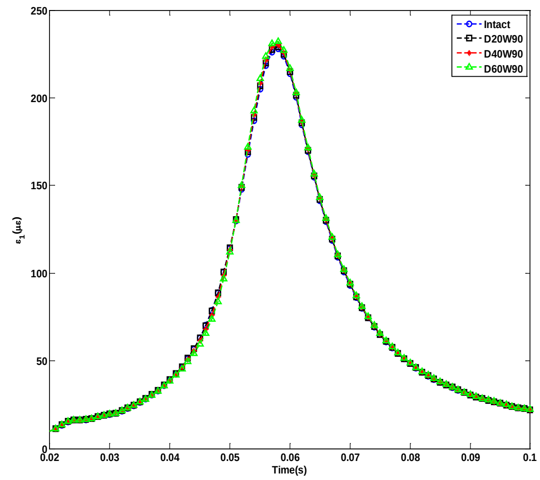

Figure 43. Strain history of sensor S2 for different damage states

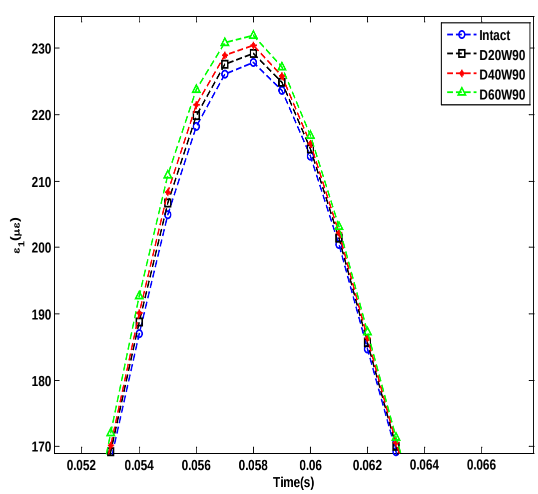

Figure 44. Zooming around the peak values for sensor S2

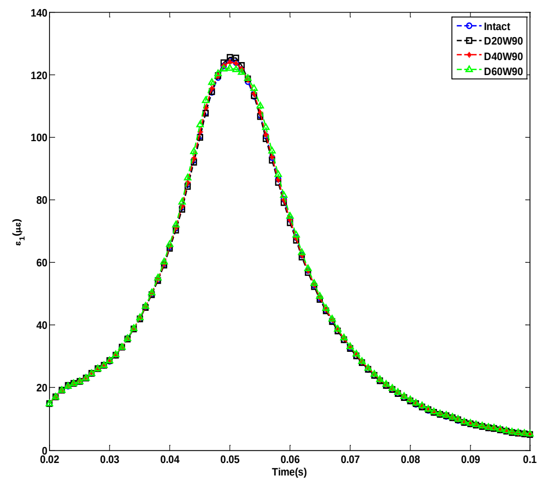

Figure 45. Strain history of sensor S17 for different damage states

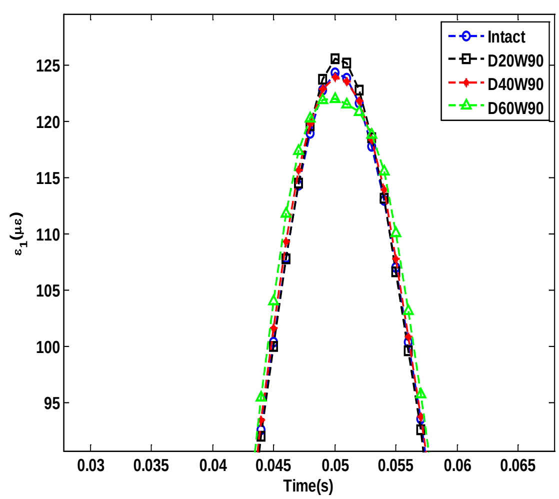

Figure 46. Zooming around the peak values for sensor S17

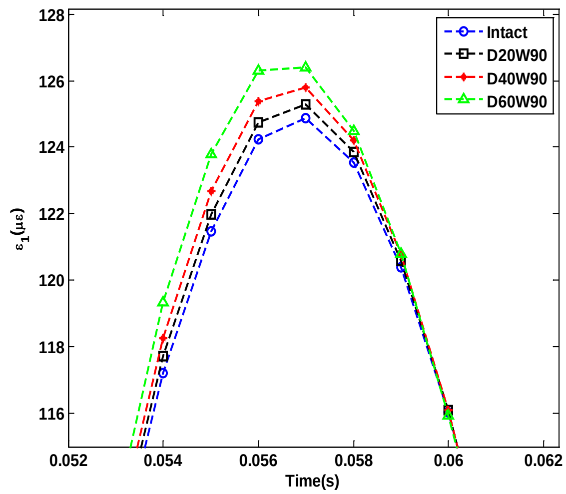

Figure 47. Zooming around the peak values for sensor S18

Fig. 48 and 49 present the variation of the maximum first principal strain (in absolute value) with respect to the percentage of modulus reduction for different damage heights. As seen in these figures, the amplitude of the strain depends on the offset of the sensor with respect to the damage zone. In fact, for a fixed reduction in the asphalt modulus, the strain amplitude increases for sensors S1 and S2 but the behavior changes when the sensors is located at a certain offset from the damage center. Furthermore, as it is illustrated by sensor S17, for a fixed damage height, the strain increases with the percentage of modulus reduction for the case of 20 mm but it has a decreasing trend for the two other damage lengths (40 mm and 60 mm). However, when the sensors are located along the wheel path, a unique trend was observed. In this case, the amplitude of the first principal strain increases with the damage height and the percentage of modulus reduction.

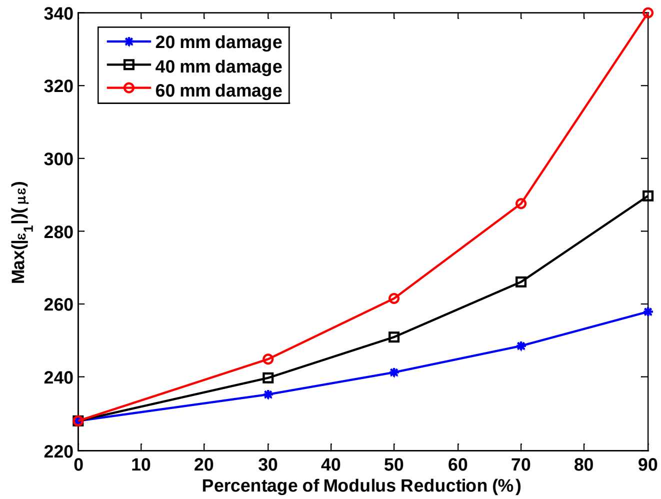

Sensor S1

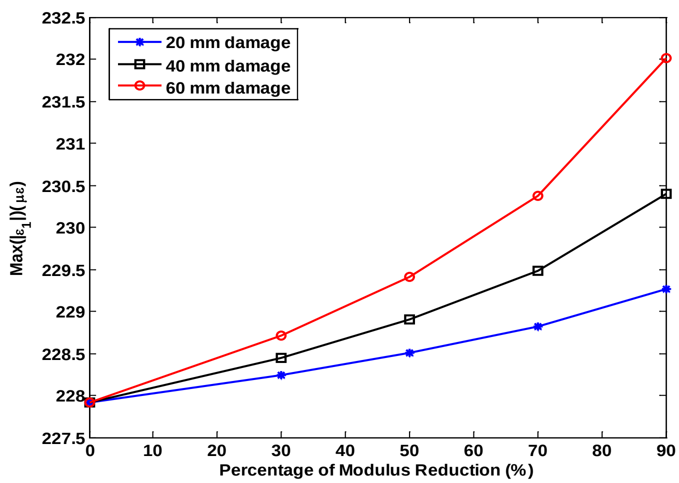

Sensor S2

Figure 48. Variation of the Maximum principal strains with the damage state for Sensors 1 and 2

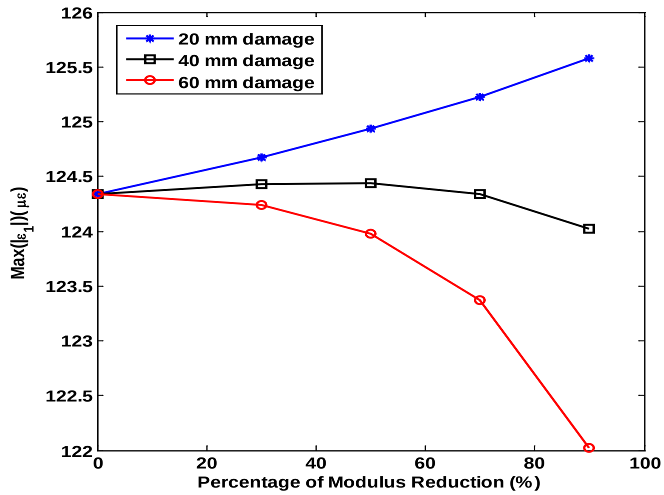

Sensor S17

Figure 49. Variation of the Maximum principal strains with the damage state for sensor 17

3. The Proposed Damage Detection Approach

The damage detection approach proposed in this work was divided into three stages. The first step was focused on generating the sensor output based on the time history of the first principal strain obtained on the previous section. Thereafter, a feature transformation method was applied to the original set of data find a reasonable relationship between the damage progression and the data of the network of sensors. Finally, a PNN classifier was used to classify the pre-defined damage classes.

3.1. Working Principle

The new class of floating-gates sensors is mainly based on the strain-energy harvested from the structure under excitation by a piezoelectric transducer. The sensors have 7 memory cells that cumulatively store the droppage in strain at a predefined threshold level. Each cell has a specific threshold level and injection rate. When the amplitude of the strain at the sensor location exceeds the threshold level of a specific gate, it starts recording the cumulative strain droppage. The injection rate is defined as the quantity of droppage in strains in 1 second at a specific memory gates.

Fig. 50 displays the procedure of obtaining the strain droppage ($\varepsilon_0 - \varepsilon_{sensor}$) at the sensor level. As it seen from the figure, the sensor strain droppage is in the form of a histogram that have different amplitude for each gate. In fact, each memory cell has an initial strain value ε_0. After applying a certain number of loading cycles, the initial strain decreases linearly with the number of cycles. Furthermore, the strain value ε_{sensor} at each gate could be written as:

$$\varepsilon_{sensor} = \varepsilon_0 - I_{gi} \sum_k \Delta t_k^{gi} \tag{26}$$

where I_{gi} is the strain injection rate and Δt_k^{gi} is the kth time intersection interval at gate gi. In this case, the shape of the histogram is random and will not follow a specific trend. The injection rates play a very important role in defining the sensor output.

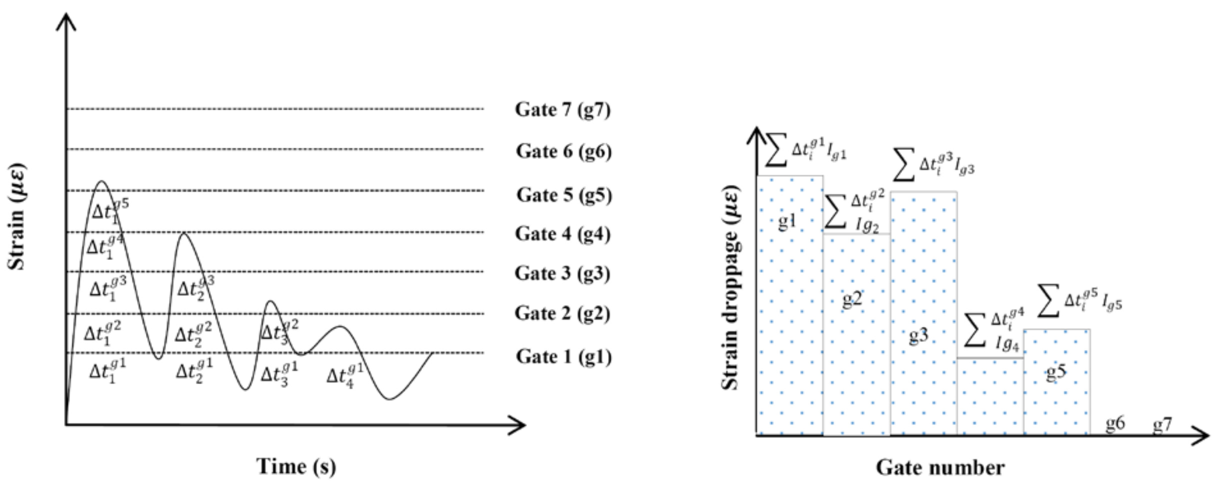

Figure 50. Procedure of obtaining the strain droppage

For the analysis, the initial strain value in each memory was set to 500 $\mu\varepsilon$. The gate injection rates as well as the strain threshold levels are displayed in Table 3. The selection of the thresholds and number of gates was based on the injection rates of the existing sensors. The activation strain of the sensor is 80 $\mu\varepsilon$ below which the device does not record any information. The maximum threshold is 200 $\mu\varepsilon$.

Table 3. The preselected strain levels and the gate injection rates considered for the analysis

Gate number	Strain threshold level ($\boldsymbol{\mu\varepsilon}$)	Injection Rates ($\boldsymbol{\mu\varepsilon/s}$)
1	80	0.001000
2	100	0.005710
3	120	0.023162
4	140	0.027822
5	160	0.006562
6	180	0.005989
7	200	0.032792

Fig. 51 presents the variation of the sensor strain at each gate versus the number of applied cycles for the intact pavement and a typical damage state. For brevity, only the results pertaining to the intact and D60W90 modes were compared for sensor S1.

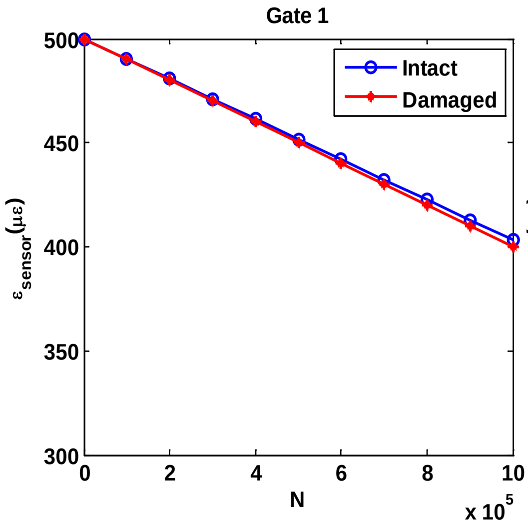
Gate 1
Intact
Damaged
500
450
400
350
300
0
2
4
6
8
10
N
x 10^5
ε_sensor(με)

(a)

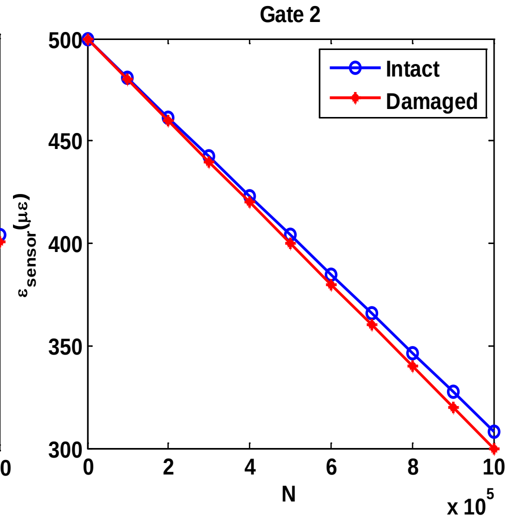
Gate 2
Intact
Damaged
500
450
400
350
300
0
2
4
6
8
10
N
x 10^5
ε_sensor(με)

(b)

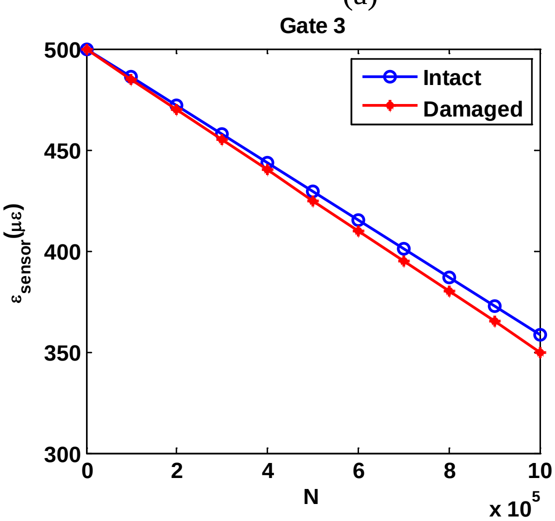
Gate 3
Intact
Damaged
500
450
400
350
300
0
2
4
6
8
10
N
x 10^5
ε_sensor(με)

(c)

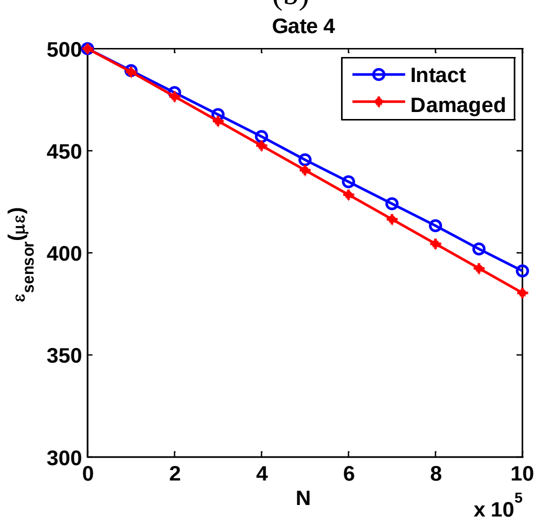
Gate 4
Intact
Damaged
500
450
400
350
300
0
2
4
6
8
10
N
x 10^5
ε_sensor(με)

(d)

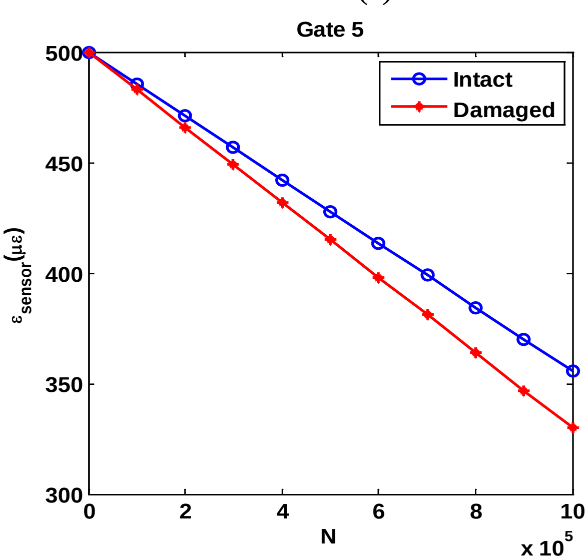
Gate 5
Intact
Damaged
500
450
400
350
300
0
2
4
6
8
10
N
x 10^5
ε_sensor(με)

(e)

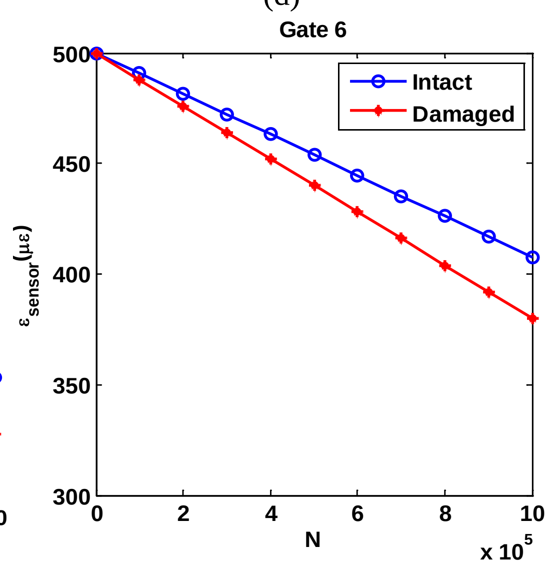
Gate 6
Intact
Damaged
500
450
400
350
300
0
2
4
6
8
10
N
x 10^5
ε_sensor(με)

(f)

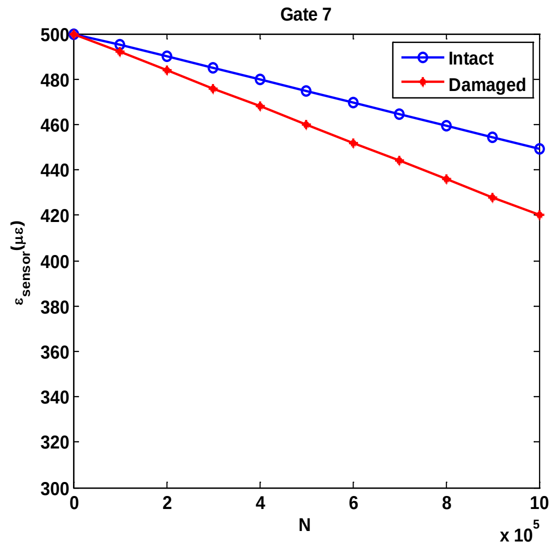

(g)

Figure 51. Strain change across sensor S1 gates

As it is seen in Fig.51, the strain varies linearly as a function of the number of cycles. In addition, the slopes of the lines corresponding to the damaged pavement are higher (in absolute value) than the intact phase. This can be explained by the fact that the amplitude of strain continuously increases at location of sensor S1 with respect to the damage progression. Thereafter, the cumulative time intersection increases with an increase in the strain amplitude. Although it can be seen that the output of the sensor changes with damage progression, there is a considerable loss of information. In fact, the sensor does not provide information about the strain distribution histograms induced by service loads which makes the task of interpreting the sensor data a challenging problem.

Alavi et al. (2016a,b,c) showed that the cumulative time histogram can be characterized by a Gaussian cumulative density function (CDF). A CDF is fully defined by only two parameters: the mean and the standard deviation of the distribution. These parameters were shown to be good indicators for damage detection (Alavi et al.2016a). On the other hand, when the gates have variable injection rates, the CDF fit will not work. Accordingly, in this work, a Gaussian mixture model (GMM) was proposed to fit the cumulative droppage of the strain at the sensing nodes. The GMMs are very powerful tools to adequately describe many types of data. In fact, certain models exhibits a multimodality that are poorly describes by a single Gaussian distribution. In the case of different injection rates, the output histogram is expected to have different rate of variation resulting in multiple maxima. Therefore, a multi-modal Gaussian mixture model can be a good fit for the data. The probability density function (PDF) of a GM distribution is given by the following expression:

$$p(x) = \sum_{k=1}^{M} \frac{c_k}{\sqrt{2\,\pi\,\sigma_k{}^2}} \exp\left[-\frac{1}{2}\left(\frac{x-\mu_k}{\sigma_k}\right)^2\right] \quad (27)$$

where: μ_k, σ_k $(k = 1..M)$ are mixture component parameters (mean and standard deviation) and c_k ae the mixture weights. The mixture weights of the PDF should satisfy the following condition:

$$\sum_{k=1}^{M} c_k = 1 \quad (28)$$

The strain droppage histogram was fitted by a bimodal GMM as follows:

$$\Delta\varepsilon(g) = \left(\sum_{i=1}^{7} \Delta\varepsilon_i\right) \sum_{k=1}^{2} \frac{\alpha_k}{\sqrt{2\,\pi\,\sigma_k{}^2}} \exp\left[-\frac{1}{2}\left(\frac{g-\mu_k}{\sigma_k}\right)^2\right] \quad (29)$$

where g is the gate number, (μ_k, σ_k) are the mixture components parameters, α_k is a parameter that represents the mixture weights and $\Delta\varepsilon_i$ is the cumulative droppage in strain at gate number i. Eq. (29) has 6 parameters to estimate: $(\mu_k, \sigma_k, \alpha_k)$, k=1,2. These parameters were obtained based on the 7 values of each gate of the sensor. Fig. 20 displays the obtained GMM fit of the data at sensor S1.

1 million traffic cycle was applied to the pavement in order to get a significant droppage of the sensor output data. It is important to mention that the injection rates could be modified using an additional resistance in parallel with the internal resistance of the sensor. Therefore, for a fatigue

analysis, the impedance of the sensor should be increased in order to lower the gates injection rates.

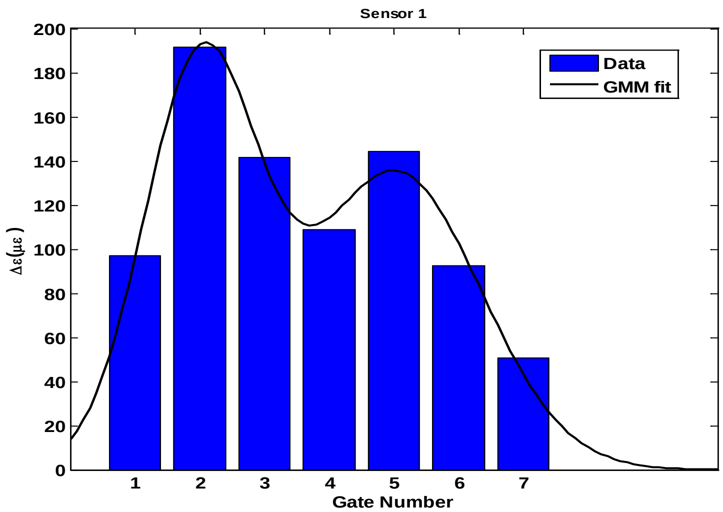

Figure 52. The GMM fit to the sensor data

As seen in Fig. 52, the output histogram presents 2 peaks corresponding to the first two maximum strain drops. It is important to mention that the maximum values do not only correspond to the gate with the highest injection rate, but it is also related to the threshold levels, the number of cycles and the strain rate variation. Fig. 53 displays the results of the GMM for different sensors. The GMM curves were plotted for the intact configurations and for D60W90 damage state. Based on the results, the GM distribution deviates from one damage states to another. According to section 3.8, the amplitude of the strain changes with damage. As a result, the cumulative time intersection changes as well and affects the variation of the strain at the sensor level.

For sensor S1, the mean (μ_1) of the first components of the GM shifts to the left (deceases) and the second mean μ_2 shifts to the right (increases). In addition, the standard deviations σ_1 and σ_2 increase with damage progression as the distribution expands. Furthermore, when the sensor is located far from the damage zone, the variation of the GMM parameters becomes less significant as indicated by sensors S2 and S3.

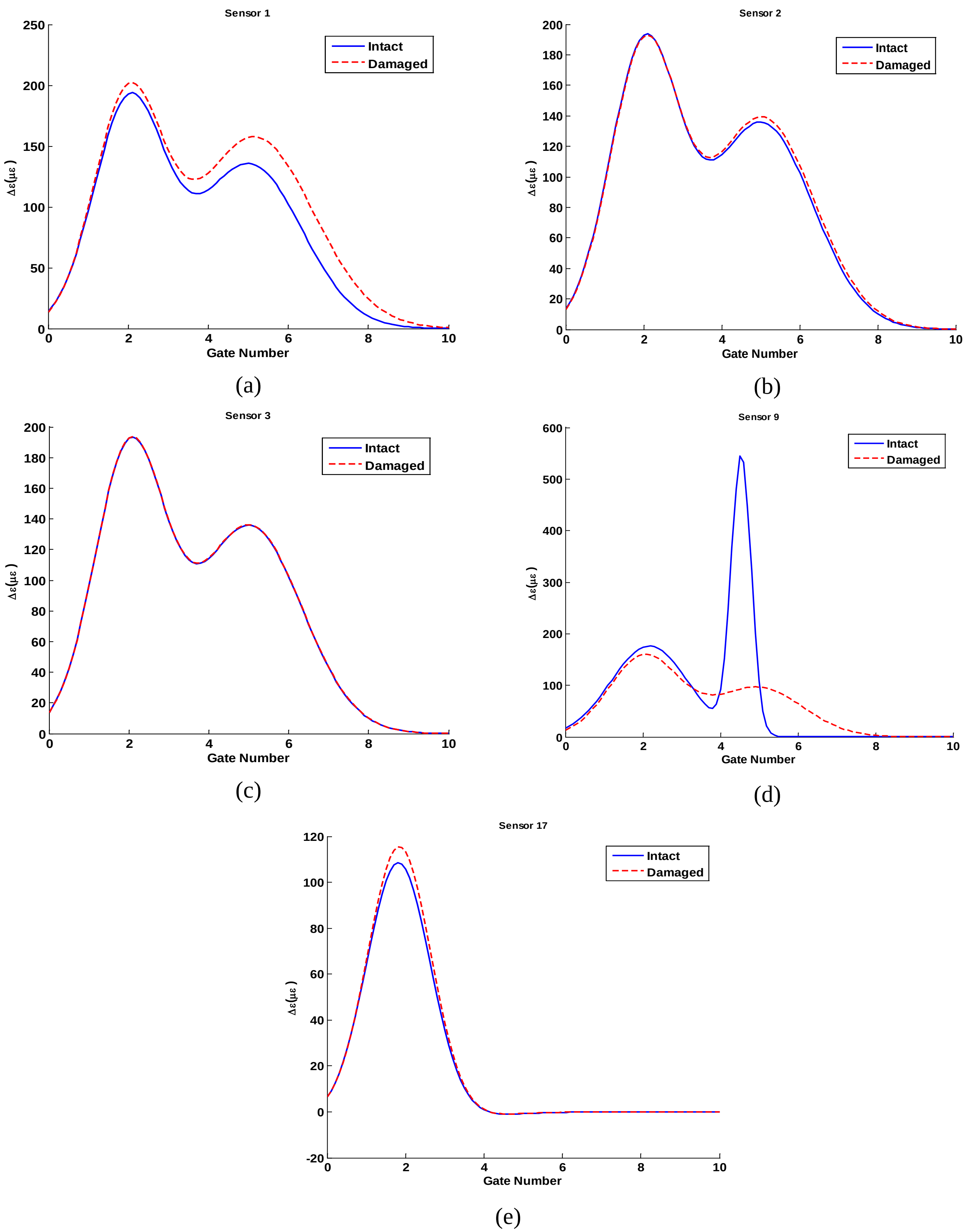

Figure 53. The GMM distributions for different sensors

An interesting observation from the output of sensor S9 is located at a 120 mm offset from the center of the pavement is thatσ_2 shows a significant variation between the intact and the damaged configurations. At the location of sensor S9, the maximum strain obtained by the FE model was below 180 $\mu\varepsilon$ for the intact configuration. Therefore, gates 6 and 7 were still inactive and they did not record any data. When the damage reaches the D60W90 damage state, the maximum strain increased to 210.94$\mu\varepsilon$ which is above the maximum threshold level of all the gates. Thus, all the gates become active. When the output of sensor S9 is fitted by the GMM, the intact configuration presents a very small σ_2 and a mean μ_2 below 6 in order to satisfy the zero strain condition described before. However, when the all the gates become active at the the last damage state (D60W90), the standard deviation of the second mixture component increases to 1.34 which is more than 16 times higher than σ_2 of the intact configuration. This considerably affects the width of the distribution.

For sensor S17, the amplitude of the strains was below 140 $\mu\varepsilon$ for both of the intact and the damaged configurations. Therefore, only the first 3 gates were active. On the other hand, all the sensors located at 180 mm offset, the strain amplitude is lower than the minimum threshold of the sensor. Thus, all the gates of these sensors remained inactive.

Based on the results, the bimodal GM parameters change due to the damage progression in the structure. Thus, the damage could be defined as function of these parameters as follows:

$$Damage = function\ (\mu_1, \sigma_1, \mu_2, \sigma_2) \tag{28}$$

However, the changes of the GM parameters are not always consistent. For example, for sensor S1, μ_1 and $,\sigma_1$ decrease and the second components (μ_2, σ_2) increase when damage progresses from the intact to D60W90 mode. For sensor S17, μ_1 and μ_2 increase and σ_1 and σ_2 decrease. Thus, it can be concluded that μ_1, σ_1, μ_2 damage, and $\sigma_2$are good damage indicators but cannot be individually used for classifying the damage state. To deal with this issue, a pattern recognition approach was developed to precisely detect the damage progression.

4. Damage classification

4.1. Probabilistic Neural Network

Computational intelligence (CI) includes a set of nature-inspired approaches can determine the model structure by automatically learning from data. CI provides alternative solutions to overcome the limitations of the traditional mathematical modeling (Alavi et al., 2016b). These limitations might be associated with the uncertainties during the process, the complexity or the stochastic nature of the process. Among different CI techniques, artificial neural network (ANNs), support vector machines (SVM) and fuzzy inference system (FIS) have been widely used in the field of damage detection (Szewezyk and Hajela 1994; Wu et al. 1992; Masri et al. 1993; Elkordy et al. 1993; Zhao et al. 1998). Major drawbacks of the widely-used ANNs are its ‘black box’ nature, the proneness to overfitting, and the time-consuming iterative procedure required during training of the network to obtain the optimal learning parameters (Yan and Miyamoto, 2003). To overcome such limitations, PNN has been proposed by Specht (1990). One advantage of PNNs is that it does not have a separate training phase which makes the execution faster than the conventional neural networks.

PNN is derived from standard Bayes classification and classical estimators for PDF. It is commonly used for pattern classification and recognition problems (Goh, 2002, Yan and Miyamoto, 2003,Adeli and Panakkat 2009). PNN uses the non-parametric density estimation scheme for density estimation based on the Parzen window technique. The Bayes formula can be expressed as follows:

$$P(\omega_j \mid x) = \frac{p(x \mid \omega_j) P(\omega_j)}{p(x)} \tag{29}$$

where $P(\omega_j|x)$is the posterior probability, $P(\omega_j)$ is the prior probability and $P(x|\omega_j)$ is the likelihood of ω_j with respect to x. The Bayes decision rule is based on the maximization of the posterior probability. As the evidence p(x) is independent of the class label, then the decision rule can be determined by estimating the likelihood probability for each class and priors.

The prior probabilities $P(\omega_j)$ can be calculated based on training dat. Thus, the only remaining unknown in the Bayes formula is the posterior probability. This class conditional probability could be estimated using the non-parametric density estimation scheme via the Parzen windows approach. More details about PNN can be found in (Duda, Hart, and Stork 2000, Cristopher and Bishop, 2006). Assuming we have N training samples, $\{x_1,\ldots,x_N\}$,divided into c classes, each of which d dimensional, and the h is the length of side of hypercube, the estimation of density at a point xin the d dimensional space is:

$$p(x) = \frac{1}{N} \sum_{n=1}^{N} \frac{1}{h^d} k(\frac{\mathbf{x} - \mathbf{x}_n}{h}) \tag{30}$$

In Eq. (30), $k((\mathbf{x} - \mathbf{x}_n)/h)$ is the kernel function that is used to count the number of patterns located inside the volume of the hypercube of volume V = h^d.

Similarly, the class conditional density of x given $\omega_j$can be calculated as follow:

$$P(x|\omega_j) = \frac{1}{N_j} \sum_{n=1}^{N_j} \frac{1}{h^d} \ k\left(\frac{x - x_n^j}{h}\right) \tag{31}$$

When a Gaussian as kernel function is used, the final estimation becomes:

$$P(x|\omega_j) = \frac{1}{N_j} \sum_{n=1}^{N_j} \frac{1}{\sigma^d} \frac{1}{(2\pi)^{\frac{d}{2}}} \exp(-\frac{1}{2} \frac{\left\|x - x_n^j\right\|^2}{\sigma^2}) \tag{32}$$

The precedent expression can be written as follow:

$$P\left(x\middle|\omega_j\right) = \frac{1}{N_j(2\pi)^{\frac{d}{2}}\sigma^d}\sum_{n=1}^{N_j}\exp(-\frac{\left\|x - x_n^j\right\|^2}{2\,\sigma^2}) \tag{33}$$

where N_j is the number of training patterns of class ω_j,σ is called the smoothing parameter that describes the spead of the Gaussian window function, and x_n^j is the n^th pattern belonging to class ω_j. The feature vectors x_n represent the center of the Gaussian window. The smoothing parameter σneed to be determined experimentally.

A typical PNN with a 4-layer architecture is shown in Fig. 54. The network is constructed by the following layers: input layer, pattern layer, summation layer, and output layer. The input layer consists of d input unit, which corresponding to the d features. Each input unit is connected to the each of the n pattern units (Alavi et al., 2016b). Each pattern unit will apply a dot product with its weighted vector $w_k$on x, yielding the *net activation* or simply *net*:

$$net_k = \mathbf{w}_k^t\mathbf{x} \tag{34}$$

The nonlinear function called activation function or transfer function will then transfer the net activation to the output to summation layer:

$$\text{actiavtion function} = e^{net_k - 1/\sigma^2} \tag{35}$$

Notice that the activation function has the same form to the Gaussian kernel:

$$e^{(net_k - 1)/\sigma^2} = e^{-(\mathbf{x}^t\mathbf{x} + \mathbf{w}_k^t\mathbf{w}_k - 2\mathbf{w}_k^t\mathbf{x})/2\sigma^2} = e^{-(\mathbf{x}-\mathbf{w}_k)^t(\mathbf{x}-\mathbf{w}_k)/2\sigma^2} \propto k(\frac{\mathbf{x}-\mathbf{w}_k}{h}) \tag{36}$$

Each neuron in the summation layer will sum these local estimates the PDFs of a single population. Thereafter, if the prior probabilities are the same and the cost functions of making an incorrect decision are the same, for all classes, the decision layer classifies according the Bayes decision rule as follows:

$$c(x) = \underset{j=1..c}{\operatorname{argmax}}\, p\left(x\middle|\omega_j\right) \tag{37}$$

When the priors and the cost functions are different between classes, the classification decision becomes:

$$c(x) = \underset{j=1..c}{\operatorname{argmax}}(p\left(x\middle|\omega_j\right)\ P\left(\omega_j\right)L_j \tag{38}$$

where L_j is the loss function associated with the misclassification of the input vector. The training of PNN is very fast, and it guaranteed the convergence to an optimal classifier as the size of training samples increases. Also, PNN does not have local minima issues. However, one major challenge is to find the optimal smoothing parameter σ. A very small σ will produce many empty hypercube and in overfitting problems. On the other hand, if window width is too large, the PNN classifier may under-fit the data as it cannot present some important local variation. Therefore, the accuracy of the PNN classifier is highly dependent on the choice of the smoothing parameter (Alavi et al., 2016b).

As mentioned before, 32 sensors were defined on the surface of the pavement. However, only 15 sensors were considered in this analysis for the following two reasons:

- The maximum strain at the 180 mm offset set of sensors is below the minimum threshold of the sensor.
- The difference on the strain peak value for last 3 sensors of each set between two damage states of each set is very low.

Therefore, only sensors S1, S2, S3, S4, S5, S9, S10, S11, S12, S13, S17, S18, S19, S20, and S21 were used in the analysis.

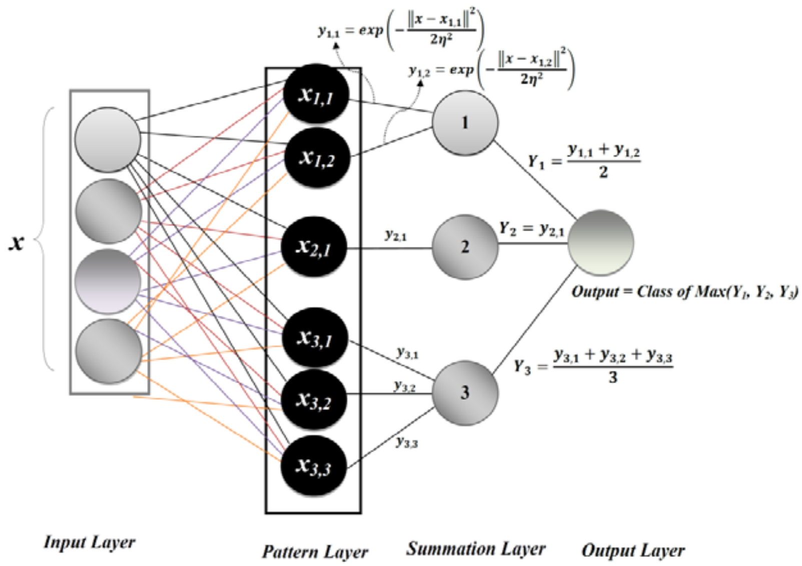

Figure 54. A typical architecture of PNN

Furthermore, the damage states were divided into 4 general classes as follows:

ω_1: Intact structure

ω_2: D20W30, D20W50, D20W70, D20W90

ω_3: D40W30, D40W50, D40W70, D40W90

ω_4: D60W30, D60W50, D60W70, D60W90

Each sensor represents a pattern for the classifier, therefore the total number of data is: 15 × 13 = 195. The performance of the developed models was measured using Detection Rate (DR):

$$DR = \frac{Number\ of\ Patterns\ Correctly\ Classified}{Total\ Number\ of\ Patterns} \qquad (39)$$

4.2. Performance of the Initial Features

The initial feature vectors were defined based on the GMM parameters (μ_1, σ_1, μ_2, and σ_2). These parameters were used to characterize the initial input vector $\underline{x}$ as follows:

$$\underline{x} = [x_1 x_2 x_3 x_4]^{\mathrm{T}} \tag{40}$$

where:

$$\begin{cases} x_1 = \mu_1 \\ x_2 = \sigma_1^2 \\ x_3 = \mu_2 \\ x_4 = \sigma_2^2 \end{cases} \tag{41}$$

As indicated by Eq. (40), the initial problem has 4 dimensions. Thus, 195 4-dimenstional patterns were used for the classification. The total number of data was divided into 3 sets:

- 70 % training = 137 data sets
- 15 % validation = 29 data sets
- 15 % testing = 29 data sets

As one would expect, these 4 initial features provided very low accuracy on the validation and testing data. The maximum detection rates for the validation and testing data were 27.58% and 13.79%, respectively. Fig. 55 displays the results of the classification in the validation set as a function of the PNN smoothing parameter (σ_{PNN}). Multiple iterations were performed by varying the smoothing parameter in order to find the optimal value that gives the best accuracy on the training and validation sets. The best configuration was then applied to un-seen testing data. As seen in Fig. 23, the best detection rate was obtained when the optimal smoothing parameter is between 1 and 10. Hence, the optimum value of σ_{PNN} is equal to 1.

Later, a Principal Component Analysis (PCA) was performed on the initial set of patterns in order to visualize the data along its first two principal components. This method can reduce a high-dimensional space to a lower-dimensional space that optimally describes the highest variance of the data.

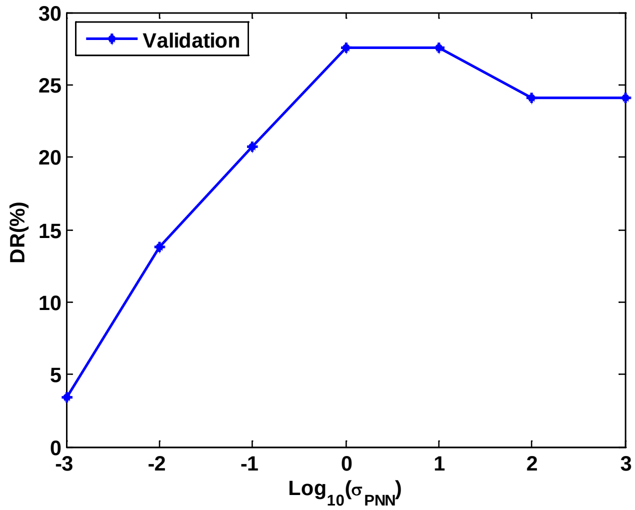

Figure 55. Accuracy versus smoothing parameter for the validation set

Fig. 56 displays the original input data x project on the two first principal components. The obtained eigen values of the covariance matrix are: $\lambda_1 = 152.49$, $\lambda_2 = 1.61$, $\lambda_3 = 0.02$, $\lambda_4 = 1.57E-04$. Hence, the first two components represent 99.99 % of the data. The detection accuracy using the reduced feature vector: $\underline{x'} = [x_1 x_2]^T$ was increased from 13.79 % to 34.48 % for the testing data. Furthermore, as seen in Fig. 56, the defined 4 damage classes overlap intensively which results in low detection accuracy.

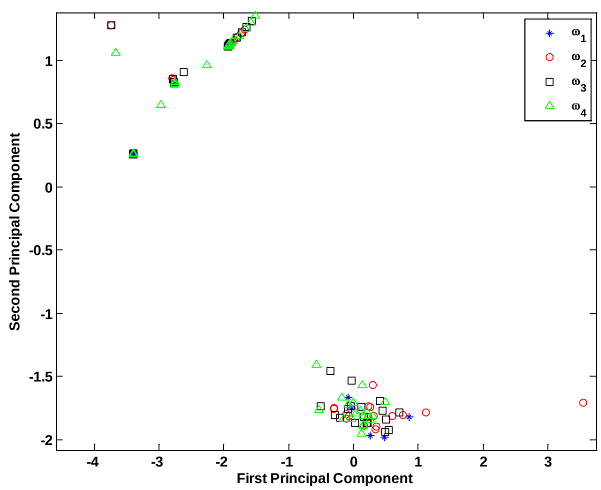

Figure 56. Projection of the featured data onto the first two principal components

4.3. Data Fusion Model

4.3.1. Feature Transformation

According to the preliminary results, the initial input feature vector $\underline{x}$ does did not contain enough information to separate classes. Hence, a new strategy was defined to improve the damage detection performance. On its basis, it was decided to fuse both the information provided by one sensor and all the information supplied by the other sensors in that specific sensor layout. This approach is also known as the' group effect' of sensors (Alavi et al. 2016a,b,c). In this case, even if one sensor does not sense the damage, the group effect (sensor network) will help detect the damage classes. Fig. 57 summarizes the proposed method for the data fusion model.

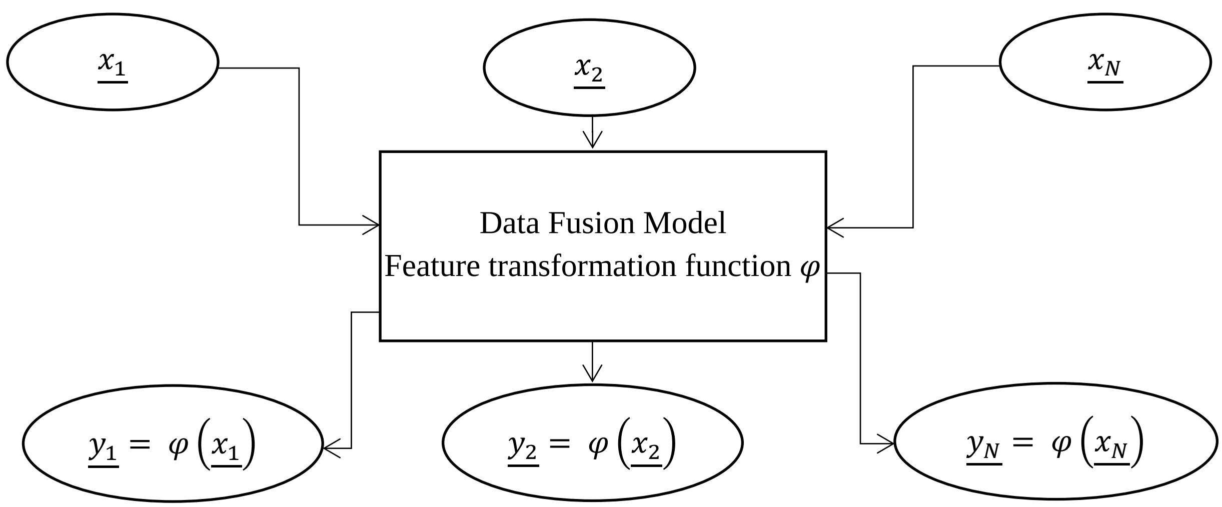

Figure 57. Data fusion model

The proposed feature transformation φ could be written as follows:

$$\varphi: \mathbb{R}^4 \xrightarrow{feature\ transformation} \mathbb{R}^{10}$$

$$\underline{x} = [x_1 x_2] \xrightarrow{\varphi} \underline{y} = [y_1 y_2 y_3 y_4 y_5 y_6 y_7 y_8\, y_9 y_{10}] \tag{42}$$

The new set of input parameters were introduced to the formulation of the damage state as follows:

$$\underline{y} = \begin{cases} y_1 = \frac{x_1 - x_{1_{\text{ave}}}}{x_{1_{\text{STD}}}} \\ y_2 = \frac{x_2 - x_{2_{\text{ave}}}}{x_{2_{\text{STD}}}} \\ y_3 = \frac{x_3 - x_{3_{\text{ave}}}}{x_{3_{\text{STD}}}} \\ y_4 = \frac{x_4 - x_{4_{\text{ave}}}}{x_{4_{\text{STD}}}} \\ y_5 = \frac{x_1 - x_{1_{\text{STD}}}}{x_{1_{\text{ave}}}} \\ y_6 = \frac{x_2 - x_{2_{\text{STD}}}}{x_{2_{\text{ave}}}} \\ y_7 = \frac{x_3 - x_{3_{\text{STD}}}}{x_{3_{\text{ave}}}} \\ y_8 = \frac{x_4 - x_{4_{\text{STD}}}}{x_{4_{\text{ave}}}} \\ y_9 = \frac{(x_1 + x_3) - (x_{2_{\text{ave}}} + x_{4_{\text{ave}}})}{x_{1_{\text{ave}}} + x_{3_{\text{ave}}}} \\ y_{10} = \frac{(x_2 + x_4) - (x_{1_{\text{ave}}} + x_{3_{\text{ave}}})}{x_{2_{\text{ave}}} + x_{4_{\text{ave}}}} \end{cases} \tag{43}$$

where,

- x_i: The i[th] feature of the initial feature vector,
- $x_{i_{\text{ave}}}$: The average of x_i for all patterns corresponding to a specific damage state,
- $x_{i_{\text{STD}}}$**:** The standard deviation of x_i for all patterns corresponding to a specific damage state.

The new defined features y_i (i=1..10) were derived from the conventional z-score functions. In fact, features y_1 to y_4 are the z-score functions and features y_5 to y_{10} are functions that are inspired by the form of the conventional z-score function. All the y_i(i=1..10) were based on the average and the standard deviation of all patterns for a specific damage state.

4.3.2. Feature Selection

The new features were expected to increase the 'distance' between classes especially between two consecutive damage states. The word distance here refers to Euclidian distance between two features in the d-dimensional space belonging to two different classes. Furthermore, by increasing the dimensionality of the problem from 4 to 10, the accuracy is more likely to increase. However, increasing the number of features may also lead on the curse of dimensionality. Therefore, different feature selection methods were used to tackle this problem. In this work, sequential forward selection (SFS), sequential backward selection (SBS) and exhaustive search (brute-force) algorithms were used to select the best set of features (Aha and Bankert, 1995; Zongker and Jain, 1996; Weston et al., 2000; MathWorks, 2016).

SFS:

SFS sequentially add the best feature y^+ that maximizes the objective function $J(Z + y^+)$. The SFS algorithm works as follows (MathWorks, 2016):

1. Start with the empty set $Z_0 = \{\emptyset\}$

2. Select the next best feature: $y^+ = \underset{x \notin Z_k}{argmax}(J(Z_k + x))$

3. Update $Z_{k+1} = Z_k + x^+$; $k = k + 1$

Go to 2

Table 4 displays the sets selected by the SFS algorithm and their performances for each step. The best accuracy on the training, validation and testing data was obtained using the feature vectors Z_8 or Z_9 selected as follows:

$$Z_8 = \{y_9, y_1, y_2, y_3, y_4, y_5, y_6, y_7\} \quad (44)$$

$$Z_9 = \{y_9, y_1, y_2, y_3, y_4, y_5, y_6, y_7, y_8\} \quad (45)$$

The detection rate accuracy using the feature vectors Z_8 or Z_9 was 100%, 96.55% and 93.10% for the training, validation and testing data, respectively. The optimal smoothing parameter was obtained for each iteration of the algorithm.

Table 4. Features selected by SFS and their corresponding detection rates

Set Number	Features	Training Accuracy (%)	Validation Accuracy (%)	Testing Accuracy (%)
1	$\{y_9\}$	94.89	89.65	89.65
2	$\{y_9, y_1\}$	100	89.65	93.10
3	$\{y_9, y_1, y_2\}$	100	79.31	93.10
4	$\{y_9, y_1, y_2, y_3\}$	100	79.31	93.10
5	$\{y_9, y_1, y_2, y_3, y_4\}$	100	79.31	93.10
6	$\{y_9, y_1, y_2, y_3, y_4, y_4\}$	100	82.75	93.10
7	$\{y_9, y_1, y_2, y_3, y_4, y_4, y_5\}$	100	82.75	93.10
8	$\{y_9, y_1, y_2, y_3, y_4, y_5, y_6, y_7\}$	100	96.55	93.10
9	$\{y_9, y_1, y_2, y_3, y_4, y_5, y_6, y_7, y_8\}$	100	96.55	93.10
10	$\{y_9, y_1, y_2, y_3, y_4, y_5, y_6, y_7, y_8, y_{10}\}$	100	96.55	89.65

SBS:

This method sequentially removes the worst feature y^-that least reduces the objective function $J(Z - y^-)$. The SBS algorithm works as follows (MathWorks, 2016):

1. Start with the full set $Z_0 = \underline{y}$,

2. Remove the worst feature: $y^- = \underset{x \in Z_k}{\operatorname{argmax}}(J(Z_k - x))$

3. Update $Z_{k+1} = Z_k - x-$*;* $k = k + 1$*.*

Go to 2

Table 5 displays the sets selected by the SBS algorithm for each step. The best accuracy on the training, validation and testing data was obtained using the feature vectors Z_1, Z_2 or Z_3, where:

$$Z_1 = \{y_2, y_3, y_4, y_5, y_6, y_7, y_8, y_9, y_{10}\} \tag{46}$$

$$Z_2 = \{y_3, y_4, y_5, y_6, y_7, y_8, y_9, y_{10}\} \tag{47}$$

$$Z_3 = \{y_3, y_4, y_5, y_6, y_7, y_8, y_9\} \tag{48}$$

The best detection accuracy was 100%, 96.55%, 93.10% for the training, validation and testing data, respectively. Multiple iterations were performed for each iteration to find the optimal smoothing parameter. Therefore, the optimal set extracted by the SBS algorithm is Z_3 which has 7 dimensions.

Table 5. Features selected by SBS and their corresponding detection rates

Set Number	Features	Training Accuracy (%)	Validation Accuracy (%)	Testing Accuracy (%)
1	$\{y_1, y_2, y_2, y_3, y_4, y_5, y_6, y_7, y_8, y_9, y_{10}\}$	100	96.55	89.65
2	$\{y_2, y_3, y_4, y_5, y_6, y_7, y_8, y_9, y_{10}\}$	100	96.55	93.10
3	$\{y_3, y_4, y_5, y_6, y_7, y_8, y_9, y_{10}\}$	100	96.55	93.10
4	$\{y_3, y_4, y_5, y_6, y_7, y_8, y_9\}$	100	96.55	93.10
5	$\{y_4, y_5, y_6, y_7, y_8, y_9\}$	100	96.55	89.65
6	$\{y_5, y_6, y_7, y_8, y_9\}$	100	96.55	86.20
7	$\{y_6, y_7, y_8, y_9\}$	100	96.55	86.20
8	$\{y_7, y_8, y_9\}$	100	96.55	86.20
9	$\{y_8, y_9\}$	98.54	93.10	86.20
10	$\{y_9\}$	94.89	89.65	89.65

Exhaustive search:

The main limitation of SFS pertains to the fact that it is unable to remove feature that become obsolete after the addition of other features. Similarly, SBS cannot reevaluate the usefulness a removed feature on the selected set (Weston et al., 2000). Both algorithms are suboptimal. Therefore, an exhaustive search algorithm was performed. It was decided to select the best 3 features that give the best classification accuracy. As the problem has 10 dimensions, the algorithm performed $C_{10}^{3} = 120$ iterations in order to find the best set of 3 features. One the best obtained sets that gives the best accuracy is:

$$S_{optimal} = \{y_4, y_7, y_9\} \tag{49}$$

The detection rate for the training, validation and testing data are equal to 100%, 96.55% and 93.10%, respectively. Fig. 58 displays the confusion matrixes. A confusion matrix is a table that displays the performance of the classification. The rows represent the predicted class and the columns represent the actual class. As observed from the confusion matrixes, only 2 patterns were misclassified in the testing set and 1 pattern in the validation set. The obtained optimal smoothing parameter was 0.01.

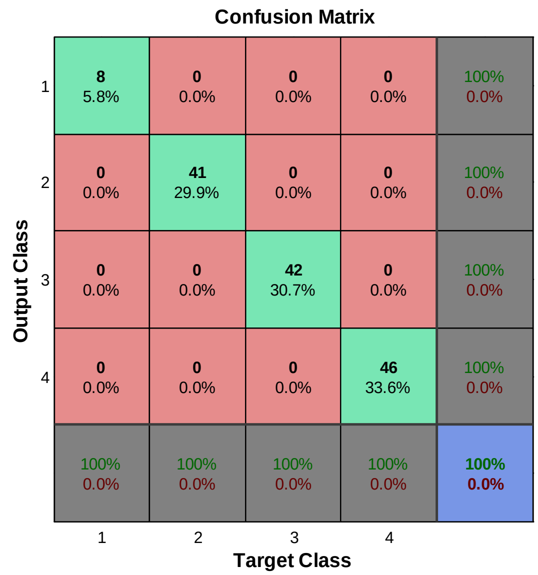

(a) Training data

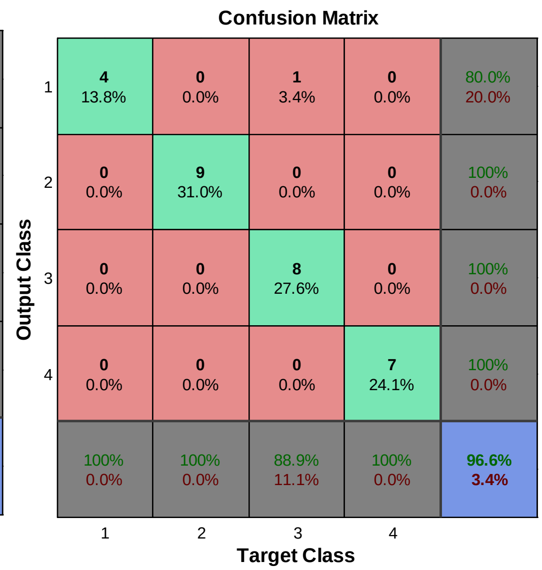

(b) Validation data

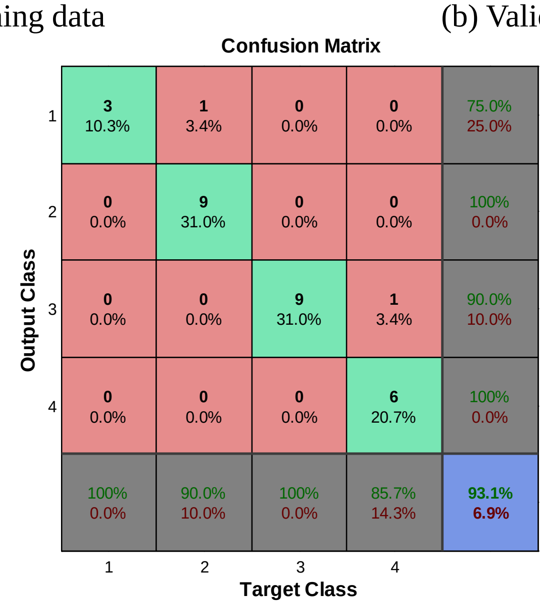

(c) Testing data

Figure 58. Confusion matrixes for the best features selected by the exhaustive search method

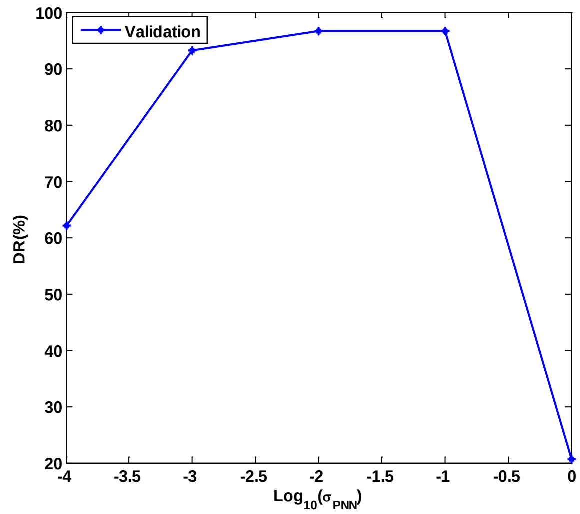

Figure 59. Accuracy versus smoothing parameter for the validation set using the exhaustive search method

The new set of features based on the data fusion model has enhanced the performance of the detection rate from 13.79 % to 93.1 % on the testing set. This new set of predictors was inspired form the conventional z-score function which is based on the average and standard deviation of a group (class) of patterns. These parameters describe the mean and the standard deviation of a certain class. Fig. 60 shows the distribution of the optimal set patterns. As seen in this figure, the classes are more separable compared to the initial input feature vectors.

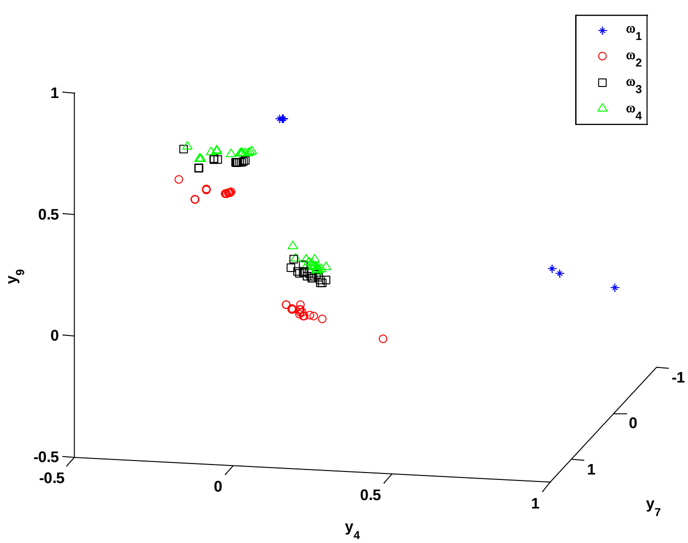

Figure 60. Distribution of the optimal set patterns

4.4. Uncertainty Analysis

In this work, the sensor data was simulated using the strain history provided by the FE modeling of the pavement under different damage scenarios. However, different sources of uncertainties can contribute to the increasing of the error between the FE modeling and the real structural behavior (Haukaas and Gardoni, 2011). On this basis, an uncertainty analysis can enhance the reliability of the proposed damage detection approach. To this aim, the input data was polluted using a Gaussian noise with 5 different levels: 10%, 20%, 30%, 40% and 50%. The best set of predictors $S_{optimal}$ was used in the noise pollution verification phase. Thereafter, the PNN was run for the different noise levels. For each case, the optimal smoothing parameter was calculated. Table 6 presents the results of the uncertainty analysis. Fig. 61 displays the detection rate accuracy as a function of the noise level using the optimal smoothing parameter. As seen in Table 5 and Fig. 61, the performance of the models remains satisfactory up to a 30% noise level. The detection rates for a noise level below or equal to 30 % are above 82 % for all of the training, validation and testing sets.

Table 6. The damage detection performance for various noise levels using the optimal set of features

Noise Level	Optimal smoothing parameter	Damage Detection Performance (%)		
		Training	Validation	Testing
10%	1E-2	100	96.55	89.65
20%	1E-2	100	82.75	86.20
30%	1E-2	100	86.20	86.20
40%	1E-1	87.59	72.41	75.86
50%	1E-2	100	72.41	75.86

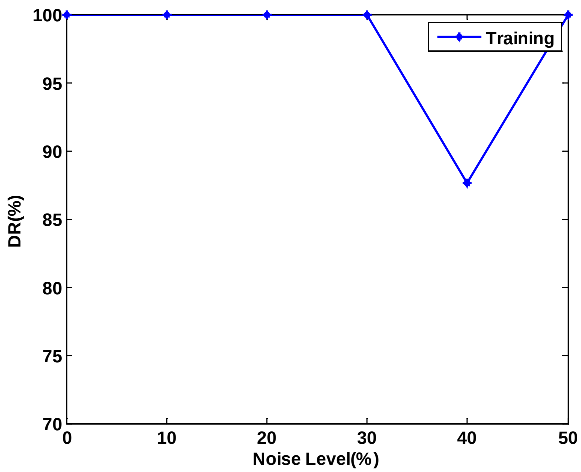

(a) Training data

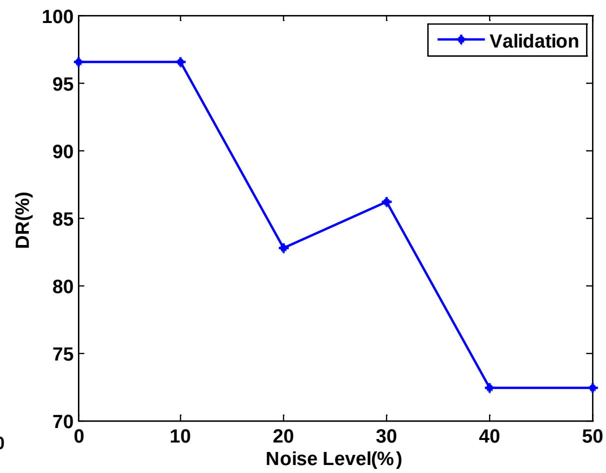

(a) Validation data

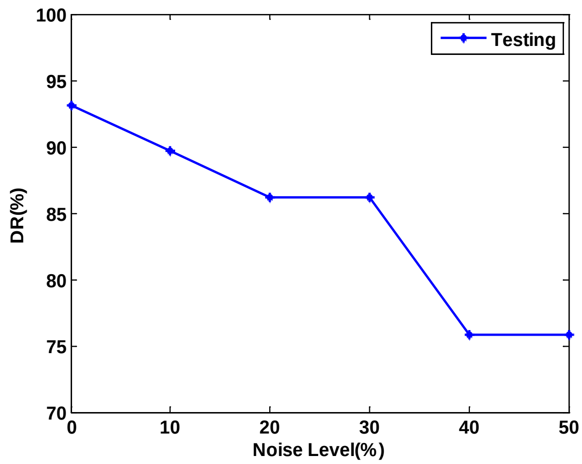

(c) Testing data

Figure 61. Damage detection accuracy for different noise levels

5. Summary and Conclusions

This work presents a new approach for pavement health monitoring based on a self-powered surface sensing technology. The self-powered sensors operate by harvesting the strain energy from the host structure and recording the cumulative droppage of the strain. Each sensor has seven memory gates for data storage. Each gate has an activation threshold level from which the sensor start recording the cumulative droppage of the strain. Moreover, each gate has a specific injection rate which controls the speed of the variation of the strain (strain droppage) at a specific timeframe. These injection rates can be modified by adding load resistance on the sensor interface board depending on the nature of the application. The difference between the previously used sensors is the variability of the injection rates between the gates which makes the interpretation of the sensor data more complicated. Therefore, a new strategy was proposed for data fitting and interpretation of the trends. The main focus is on the detection of bottom up cracking in the AC pavements using sensors located near the surface of the layer. In particular, such surface sensing technology is important for the monitoring of existing pavements. In order to verify the performance of the proposed method, 3D FE models of the pavement structure were created using ABAQUS. Subsequently, the principal strain time histories were extracted for different sensing nodes on the surface of the AC layer. The pavement was subjected to a dynamic moving load at highway speed. The models incorporated the tire-pavement contact stress, a viscoelastic behavior for HMA, an elastic behavior with damping for base and subgrade, and a continuous moving load. The moving load was created via a DLOAD subroutine using a FORTRAN code. Thereafter, different damage scenarios were introduced to the bottom of the AC layer. The damage states were defined based on the EWM by reducing the material properties of the damaged area. The FE results show that the strain amplitude changes as a function of the damage state. In addition, the locations of sensors with respect to the damage control the change in the strain amplitude. The sensor output was calculated based on the FE strain history. Based on the results, it was found that the damage could be detected through the strain droppage of the sensor gates. Only the sensors at a specific location with respect to the damage location were sensitive to the damage progression. To tackle this problem, two different stages were considered for the performance verification of the proposed approach. At the first stage, the complicated histogram of sensor data was fitted by a bi-modal GM model in order to define initial damage indicators. The results show that the bi-modal GM parameters are good damage indicators only at specific locations. Thus, a data fusion model was proposed by defining new descriptive features from the GMM parameters. These new predictors contained the information supplied by the all the sensors at each specific sensing location. Thereafter, different feature extraction methods (SFS, SBS, Brute force) were used to check the curse of dimensionality and to select the optimal set of sensors that give the best accuracy. A PNN classification scheme was used to classify the predefined damage stages. The results showed that using the optimal set of predictor features could provide satisfactory detection rate accuracy (100% on the training data, 96.6% on the validation data and 93.1% on the testing data). Finally, an uncertainty analysis was performed to simulate the performance of the sensor under real operating conditions and to take into account the errors of the numerical modeling. A Gaussian noise with different levels was applied to the data. The detection performance remained satisfactory up to 30% noise level. While the proposed approach has provided sound results, there are still some challenges to be addressed in the future studies:

- The conducted analyses were based on discrete damage states, while cracking is a continuous phenomenon in reality. Hence, developing FE models with continuous damage propagation can result in a more realistic detection approach.
- The effect of high or low temperatures on the sensor output needs more research.
- Reliability of the sensor under different environmental and operating conditions should be evaluated more in-depth.
- Verification of the long-term performance of the proposed approach for a real-life structure is also an interesting topic for the future study.

References

Miller, J. S., and Bellinger, W. Y. (2003). “Distress identification manual for long-term pavement performance program (fourth revised edition).” Report FHWA-RD-03-031, Federal Highway Administration (FHWA), Washington, DC, 2003.

Cebon, D., 1986. Road damaging effects of dynamic axle loads. In: Proceedings of the international symposium on heavy vehicle weights and dimensions, Kelowna, BC, Canada 37–53.

Gillespie, T. D., S. M. Karimihas, D. Cebon, M. W. Sayers, M. A. Nasim, W. Hansen, and N. Ehsan. NCHRP Report 353: Effect of Heavy Vehicle Characteristics on Pavement Response and Performance. TRB, National Research Council, Washington, D.C., 1993.

Lourens, J.P., 1992. Nonlinear dynamic analysis and design of road pavements. Pretoria: Department of Transport, RR 90/030.

Huang, Y.H. Pavement Analysis and Design, 1st ed. Prentice Hall, N.J.,1993.

Yoo, P.J. and Al-Qadi, I.L., 2007. Effect of transient dynamic loading on flexible pavements. Transportation Research Record, 1990, 129–140.

Al-Qadi I.L., Loulizi A., Elseifi M., Lahouar S. 2004. The Virginia Smart Road: the impact of pavement instrumentation on understanding pavement performance. Asphalt Paving Technology, 73, 427–465.

Elseifi, M.A., Al-Qadi, I.L., and Yoo, P.J., 2006. Viscoelastic modeling and field validation of flexible pavements. ASCE Journal of Engineering Mechanics, 132 (2), 921–962.

Yang S., Ceylan H., Gopalakrishnan K., Kim S., (2014). Smart airport pavement instrumentation and health monitoring Civil, Construction and Environmental Engineering Conference Presentations and Proceedings. Paper 8.

Attoh-Okine, N., and Mensah, S. (2003). MEMS Application in Pavement Condition Monitoring-Challenges. NIST Special Publication SP, pp. 387-392.

Xue W., (2013) Integrated Transportation Monitoring System for Both Pavement and Traffic. PhD Thesis, Virginia Polytechnic Institute and State University, Blacksburg, VA.

Dong, Z. J., Li, S. L., Wen, J. Y., & Chen, H. C. (2012). Asphalt Pavement Structural Health Monitoring Utilizing FBG Sensors. Advanced Engineering Forum, Vol. 5, pp. 339-344.

Bennett, R., Hayes-Gill, B., Crowe, J. A., Armitage, R., Rodgers, D., and Hendroff, A. (1999). Wireless Monitoring of Highways. Smart Systems for Bridges, Structures, and Highways, Proceedings of the SPIE, Newport Beach, CA, March 1–2, Vol.3671, pp. 173–182.

Ceylan, H., Gopalakrishnan, K., Kim, S., Taylor, P. C., Prokudin, M., and Buss, A. F. (2013). Highway Infrastructure Health Monitoring Using Micro-Electromechanical Sensors and Systems (MEMS). Journal of Civil Engineering and Management, Vol.19 (sup1), pp. 188-201.

Chatti K, AH Alavi, H Hasni, N Lajnef, F Faridazar - 8th RILEM International Conference on Mechanisms Cracking and Debonding in Pavements, 2016.

Alavi A.H., Hasni H., Lajnef N., Chatti K., Faridazar F., Continuous Health Monitoring of Pavement Systems Using Smart Sensing Technology. Construction and Building Materials, 2016a, 114, 719–736.

Alavi A.H., Hasni H., Lajnef N., Chatti K., Faridazar F. An Intelligent Structural Damage Detection Approach Based on Self-Powered Wireless Sensor Data. Automation in Construction, 201ba, 62, 24–44.

Alavi A.H., Hasni H., Lajnef N., Chatti K., Faridazar F., Damage Detection Using Self-Powered Wireless Sensor Data: An Evolutionary Approach. Measurement 2016c, 82, 254–283.

Huang C., Lajnef N., Chakrabartty S., Self-calibration and characterization of self-powered floating-gate usage monitors with single electron per second operational limit. IEEE Transactions on Biomedical Circuits and Systems, 2010, 57, 556-567.

Lajnef N., Chatti K., Chakrabartty S., Rhimi M., Sarkar P., Smart Pavement Monitoring System. Report: FHWA-HRT-12-072, Federal Highway Administration (FHWA), Ishington, DC, 2013.

Lajnef N., Rhimi M., Chatti K., Mhamdi L., Toward an Integrated Smart Sensing System and Data Interpretation Techniques for Pavement Fatigue Monitoring. Computer-Aided Civil and Infrastructure Engineering, 2011, 26, 513–523.

Zhou Z, Liu W, Huang Y, Wang H, Jianping H, Huang M, Jinping O (2012) Optical fiber Bragg grating sensor assembly for 3D strain monitoring and its case study in highway pavement. Mech Syst Signal Process 28:36–49

ABAQUS (2010). ABAQUS/CAE User's Manual, Version 6.10, Dassault Systèmes.

Al-Qadi, I.L., Wang, H., and Tutumluer, E., 2010. Dynamic analysis of thin asphalt pavements utilizing cross-anisotropic stress-dependent properties for granular layer. Transportation Research Record, 2154, 156–163.

Wang, H., 2011. Analysis of tire-pavement interaction and pavement responses using a decoupled modeling approach, PhD Dissertation in Civil Engineering, The Graduate College of the University of Illinois at Urbana-Champaign.

Duncan, J.M., Monismith, C.l., and Wilson, E.L., 1968. Finite element analysis of pavements. Highway Research Record, 228, 18–33.

Chopra, A.K. (2001) Dynamics of Structures, 2nd ed., Prentice Hall, Upper Saddle River, NJ.

Bathe, K.J., 1996. Finite element procedures. Englewood Cliffs, NJ: Prentice Hall.

Michalczyk, R., “Implementation of Generalized Viscoelastic Material Model in Abaqus Code”, Logistyka, vol. 6, 2011.

Siddharthan, R. V., Yao, J., and Sebaaly, P. E. (1998). “Pavement strain from moving dynamic 3D load distribution.” J. of Transp. Eng., 124(6): 557-566.

Tielking, J. T., and Roberts, F. L. (1987). “Tire contact pressure and its effect on pavement strain.” J. of Transp. Eng., 113(1): 56-71.

Wang F., and Machemehl, R. B. (2006). “Mechanistic-emperical study of effects of truck tire pressure on pavement: measured tire-pavement contact stress data.” Transportation Research Record 1947, TRB, National Research Council, Washingon D.C., 136-145.

Yue, Z. Q. and Svec, O. J. (1995). “Effects of tire-pavement contact pressure distributions on the response of asphalt concrete pavemens.” Candian J. of Civil Eng., 22(5): 849-860.

Alkasawneh, W., Pan, E., and Green, R. (2008). “The effect of loading configuration and footprint geometry on flexible pavement response based on linear elastic theory.” Road Mater. and Pavement Eng., 9(2): 159-179.

Mun, S., Guddati, M. N., and Kim, Y. R. (2006). “Viscoelastic continuum damage finite element modeling of asphalt pavements for fatigue cracking evaluation.” KSCE J. Civ. Eng., 10(2): 97-104.

Weissman S. (1999). “Influence of tire-pavement contact stress distribution on development of distress mechanisms in pavements.” Transportation Research Record 1655, TRB, National Research Council, Washington D.C., 161-167.

Perret, J., and Dumont, A. (2004). “Strain and stress distributions in flexible pavements under moving loads.” Road Mater. And Pavement Design, 5(1): 203-225.

Al-Qadi I.L., Wang H., Pavement Damage Due to Different Tire and Loading Configurations on Secondary Roads. NEXTRANS University Transportation Center, West Lafayette, Ind, 2010.

Huang, C., Abu Al-Rub, R. K., Masad, E. A., and Little, D. N. (2011). “Three-dimensional simulations of asphalt pavement permanent deformation using a nonlinear viscoelastic and viscoplastic model.” J. Mater. Civ. Eng., 23(1): 56-68.

Sarkar, A. (2015). “Numerical comparison of flexible pavement dynamic response under different axles.” Int. J. of Pavement Eng.

Shafabakhsh, G., Naderpour, H., and Motamedi, M. (2015). “Dynamic analysis and determination of maximum tensile strain of bottom asphalt concrete for different vehicle velocities.” Engineering Journal, 19(4): 107-116.

Dave, E. V., and Buttlar, W. G. (2010). “Thermal reflective cracking of asphalt concrete overlays.” Int. J. of Pavement Eng., 11(6): 477-488.

Song, S. H., Paulino, G. H., and Buttlar, W. G. (2006). “A bilinear cohesive zone model tailored for fracture of asphalt concrete considering rate effects in bulk materials.” Engineering Fracture Mechanics, 73(18); 2829-2848.

Mishnaevsky Jr., L. L (2004). “Three-dimensional numerical testing of microstructures of particle reinforced composites.” ActaMaterialia, 52: 4177-4188.

Szewezyk P., Hajela P., Damage detection in structures based on feature - sensitive neural networks. J. Comp. Civ. Engrg. ASCE 8(2) (1994) 163 - 178.

Wu X., Gahboussi J., Garrett J.H., Use of neural networks in detection of structural damage[J] . Comput. Struct. 42(4) (1992) 649 - 659.

Masri S.F., Chassiakos A.G, Caughey T.K., Identification of nonlinear dynamic systems using neural networks .J.Appl. Mech. Trans. ASME 60 (1993) 123 - 133.

Elkordy M.F, Chang K.C., Lee G.C., Neural networks trained by analytically simulated damage states. Journal of Comp in CivEngrg , ASCE 7(2) (1993) 130 - 145.

Zhao J., Ivan J.N., DeWolf J.T., Structural Damage Detection Using Artificial Neural Networks, J. Infrastruct. Syst. ASCE, 4(3) (1998) 0093-0101.

Yan B., Miyamoto A., Application of probabilistic neural network and static test data to the classification of bridge damage patterns. Proceedings of SPIE 5057, 2003, 606-617.

Specht D., Probabilistic Neural Networks. Neural Networks, 1990, 3, 109-118.

Goh A.T.C., Probabilistic neural network for evaluating seismic liquefaction potential. Canadian Geotechnical Journal, 2002, 39, 219-232.

Adeli H., Panakkat A., A probabilistic neural network for earthquake magnitude prediction. Neural Networks, 2009, 22, 1018-1024.

Duda R.O., Hart P.E., Stork D.G., Pattern Classification and Scene Analysis. second ed., New York: John Wiley &, Sons, 2000.

Cristopher M., Bishop S., (2006). Pattern Recognition and Machine Learning. Springer, London.

Zongker, D., Jain, A.: Algorithms for feature selection: An evaluation Pattern Recognition. In: Proceedings of the 13th International Conference, vol. 2, pp. 25–29, 18–22 (1996)

MathWorks (2016). MATLAB the language of technical computing, Version R2016a, MathWorks Inc., Natick, MA, USA.

Aha D.W., Bankert R.L. A comparative evaluation of sequential feature selection algorithms D. Rsher, H. Lenz (Eds.), Proceedings 5th International Workshop on Artificial Intelligence and Statistics, Ft. Lauderdale, FL (1995), pp. 1–7

Weston,J., Mukherjee,S., Chapelle,O., Pontil,M., Poggio,T. and Vapnik,V. (2001) Feature selection for SVMs. In Leen,T.K., Dietterich,T.G. and Tresp,V. (eds), Advances in Neural Information Processing Systems 13. MIT Press, Cambridge, MA.

Haukaas T., Gardoni P., Model Uncertainty in Finite-Element Analysis: Bayesian Finite Elements. J. Eng. Mech., 2011, 137(8): 519-526.